CMS Physics Analysis Summary

Contact: cms-pag-conveners-ewk@cern.ch 2010/07/22

Measurements of Inclusive W and Z Cross Sections in pp Collisions at $\sqrt{s} = 7$ TeV

The CMS Collaboration

Abstract

We present the first measurements of inclusive W and Z production cross sections in muon and electron decay channels at $\sqrt{s} = 7$ TeV, obtained using 198 nb^{-1} of pp collisions in the Compact Muon Solenoid (CMS) detector at the Large Hadron Collider (LHC). The measured inclusive cross sections are $\sigma(\mathrm{pp} \to \mathrm{W} + X \to \ell\nu + X) = 9.22 \pm 0.24(\mathrm{stat.}) \pm 0.47(\mathrm{syst.}) \pm 1.01(\mathrm{lumi.})$ nb, and $\sigma(\mathrm{pp} \to \mathrm{Z}(\gamma^*) + X \to \ell^+\ell^- + X) = 0.882^{+0.077}_{-0.073}(\mathrm{stat.})^{+0.042}_{-0.036}(\mathrm{syst.}) \pm 0.097(\mathrm{lumi.})$ nb, limited to the dilepton invariant mass range $[60, 120]$ GeV. The luminosity-independent cross section ratios are $\sigma(\mathrm{pp} \to \mathrm{W} + X \to \ell\nu + X)/\sigma(\mathrm{pp} \to \mathrm{Z}(\gamma^*) + X \to \ell^+\ell^- + X) = 10.46^{+0.99}_{-0.88}(\mathrm{stat.})^{+0.65}_{-0.56}(\mathrm{syst.})$ and $\sigma(\mathrm{pp} \to \mathrm{W}^+ + X \to \ell^+\nu + X)/\sigma(\mathrm{pp} \to \mathrm{W}^- + X \to \ell^-\nu + X) = 1.51^{+0.08}_{-0.07}(\mathrm{stat.}) \pm 0.04(\mathrm{syst.})$. The measured values agree with NNLO QCD cross section calculations and current parton distribution functions. We also present measurements of the W lepton asymmetry in three bins of pseudorapidity and the forward-backward asymmetry for di-muon pairs. Finally, we present the first study of hadronic jets produced in association with W bosons.

1 Introduction

This note describes the first measurement in pp collisions at $\sqrt{s} = 7$ TeV of the inclusive production cross section for W and Z bosons, observed via their decay to electrons and muons, and additionally presents selected cross section ratios and differential distributions. The production of W and Z bosons decaying to charged leptons is an important process to measure at the LHC, for a host of reasons: it is simultaneously a benchmark for lepton reconstruction and identification to be used in future analyses, a precision test of perturbative QCD and the parton distribution functions of the proton (PDFs), a possible estimator of integrated luminosity for proton collisions [1], and the first electroweak process to be observed at the LHC. At the LHC, QCD predictions, in next-to-next-to leading order (NNLO) in the strong coupling α_S, exist for the matrix elements describing inclusive W and Z production. When combined with recent NNLO PDFs, the cross section is predicted with a few percent uncertainty [2, 3]. The production of the W and the Z in hadron collisions has been measured at several previous experiments over a range of collision energies [4–8], and Standard Model predictions have been observed to agree well with them. The ratio of inclusive cross sections for Ws and Zs, R_{WZ}, and the ratio of cross sections for W^+ and W^-, R_{+-}, are also precisely predicted at the same level of accuracy, but do not suffer from experimental uncertainties in proton collision luminosity, which cancel, along with other uncertainties.

Measurements of differential cross sections also test Standard Model predictions. The charge asymmetry of W bosons, measured as a function of the charged lepton pseudorapidity, is a potentially powerful constraint on PDFs. The forward-backward asymmetry of di-lepton pairs is potentially sensitive to the presence of extra neutral gauge bosons. Finally, studies of the production of jets in association with W bosons test perturbative QCD calculations, as well as models of the underlying event.

The study uses 198 nb^{-1} of proton collisions collected at $\sqrt{s} = 7$ TeV in the 2010 LHC run using the CMS detector. A detailed description of CMS and its performance can be found in Ref. [9]. The systematic uncertainty on the luminosity is currently 11% [10].

For W measurements, two techniques are employed to measure with precision the missing transverse energy in the event, $\not\!\!E_T$. They are denoted by particle-flow $\not\!\!E_T$ [11] and track-corrected $\not\!\!E_T$ [12]. Both of them take advantage of the high precision of inner tracking in CMS in order to improve upon the calorimeter estimates of the deposited energies. The particle-flow strategy also attempts to perform particle identification and therefore corrects and improves the resolution depending on specific particle assumptions. Particle-flow $\not\!\!E_T$ is the baseline choice for the analyses presented in this note. As a test of robustness of the measurements, the equivalent track-corrected $\not\!\!E_T$ distributions are also presented in an Appendix.

Several large samples of simulated events are used to evaluate signal and background efficiencies and to validate our analysis techniques. Samples of electroweak processes with Z and W production, both for signal and background events, are produced with POWHEG [13–15] interfaced with the PYTHIA [16] parton-shower generator. QCD events with muons, electrons or jets likely to fake electrons in the final state are studied with PYTHIA, as well as other minor backgrounds in the analysis, like $t\bar{t}$. Generated events are processed through the full GEANT4 [17] detector simulation, trigger emulation and event reconstruction chain of the CMS experiment.

2 High-p_T muon identification and selection

The muon identification strategy followed in this note is consistent with the CMS muon quality criteria studies in [18]. For the typical range of transverse momenta explored in this analysis ($p_T < 200\,\mathrm{GeV}/c$) the muon momentum resolution is dominated by the inner tracker measurements. Events with high-p_T muons are recorded online using the Level-1 muon trigger and the high-level trigger (HLT), which require information from the muon chambers (Level-1, HLT) and the inner tracker (HLT). A trigger path with an HLT threshold of $p_T > 9\,\mathrm{GeV}/c$ in the $|\eta| < 2.1$ region is chosen as the baseline of the analysis.

A good consistency between tracker and muon detector measurements is essential to reduce the contamination from muons produced in decays in flight of hadrons and from punch-through. First, the muon must be identified by two different algorithms, one that starts from inner tracker information ("tracker muons"), and another one that starts from segments in the muon chambers ("global muons"). Second, we apply a cut of $\chi^2/ndof < 10$ on a global fit containing tracker and muon hits. Finally, we demand the presence of at least two levels of muon stations in the measurement. This latter condition ensures a sensible momentum estimate at the muon trigger level, and further suppresses remaining punch-through and sail-through candidates, which are unable to penetrate deeply in the iron yoke of CMS.

In order to ensure a precise estimate of momentum and impact parameter, only tracks with more than 10 hits and at least one hit in the pixel detector are used. Cosmics are rejected by requiring a transverse impact parameter distance to the beam spot position of less than 2 mm. Dedicated studies of muons in cosmic runs show that the high-p_T cosmic contamination after this cut is negligible in the present sample. More details and studies on muon identification in CMS at $\sqrt{s} = 7$ TeV can be found in Reference [18].

3 Measurement of the W $\rightarrow \mu\nu$ yield

W $\rightarrow \mu\nu$ events are characterized by a high-p_T isolated muon, together with a significant amount of missing transverse energy ($\not\!\!E_{\mathrm{T}}$), due to the presence of a neutrino in the final state that escapes undetected.

A full reconstruction of the W system is not possible but a mass reconstruction in the transverse plane can be performed from the measured $\not\!\!E_{\mathrm{T}}$ and the muon momentum. This transverse mass is defined as: $\mathrm{M}_T = \sqrt{2p_T(\mu)\not\!\!E_{\mathrm{T}}(1-\cos(\Delta\phi_{\mu,\not\!\!E_{\mathrm{T}}}))}$, where $\Delta\phi_{\mu,\not\!\!E_{\mathrm{T}}}$ is the azimuthal angle between muon and $\not\!\!E_{\mathrm{T}}$ directions. The resulting M_T distribution exhibits the characteristic shape of the W Jacobian peak.

We first reject events with two global muons satisfying: $p_T(\mu_1) > 20$ GeV/c and $p_T(\mu_2) > 10$ GeV/c, where $p_T(\mu_1)$ is the highest muon p_T and $p_T(\mu_2)$ is the second highest muon p_T in the event, in order to minimize the contribution from Drell-Yan events to the selected sample. Events with an identified muon in the fiducial volume $|\eta| < 2.1$ and with $p_T > 20$ GeV/c are kept.

The isolation variable for muons is defined as:

$$I^{\mathrm{rel}}_{\mathrm{comb}} = \left\{ \sum (p_T(tracks) + E_T(em) + E_T(had)) \right\} / p_T(\mu) \qquad (1)$$

where the sums are defined in a $\Delta R = \sqrt{(\Delta\phi)^2 + (\Delta\eta)^2} < 0.3$ cone around the muon direction. In this cone, $\sum p_T(tracks)$ is the sum of all transverse tracker momenta and $\sum(E_T(em) +$

$E_T(had)$) is the sum of all transverse energies of electromagnetic and hadronic deposits. The muon track and associated deposits are excluded from these sums. The muon is considered to be isolated if $I^{\text{rel}}_{\text{comb}} < 0.15$. The distribution of the isolation variable for muons satisfying all previous requirements is presented in Figure 1. The data reduction at different stages of the selection is summarized in Table 1. The acceptance of the selection cuts for $W \to \mu\nu$ events with muons emitted in the $|\eta| < 2.1$ pseudo-rapidity region is $64.1 \pm 0.2(\text{stat.})\%$, as estimated from Monte Carlo simulations.

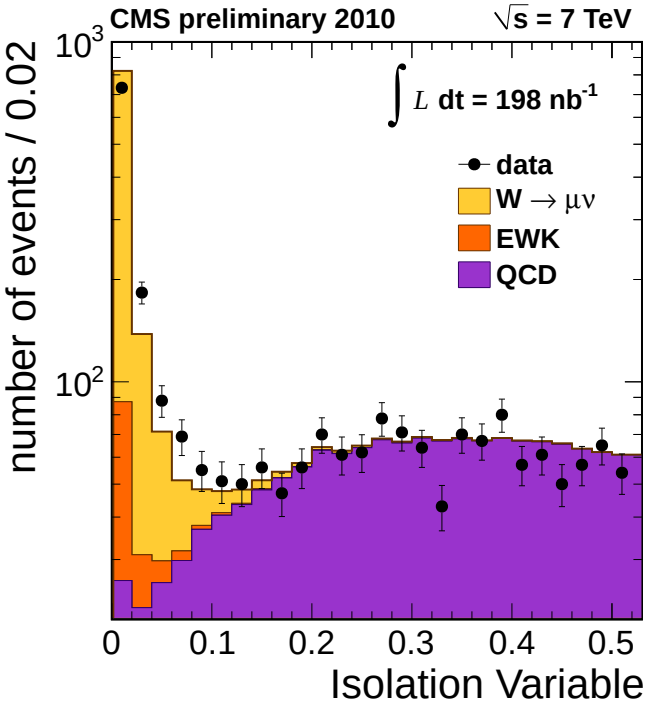

Figure 1: Distribution of the isolation variable in selected events with an identified muon of $p_T > 20$ GeV/c in $|\eta| < 2.1$. Points are data and the solid histograms the Monte Carlo predictions normalized to a total integrated luminosity of $\mathcal{L}_{\text{int}} = 198$ nb^{-1}. Electroweak backgrounds considered (EWK) are Drell-Yan, $W \to \tau\nu$, $Z \to \tau^+\tau^-$ and $t\bar{t}$.

Selection criteria	Number of events	Events with μ^+	Events with μ^-
Triggered	16567	8607	7960
Drell-Yan rejection	16277	8444	7833
Muon identification cuts	13365	6873	6492
$\|\eta\| < 2.1$ & $p_T > 20$ GeV/c	4294	2275	2019
$I^{\text{rel}}_{\text{comb}} < 0.15$	1254	757	497

Table 1: Data reduction after each selection cut applied. The experimental data sample corresponds to $\mathcal{L}_{\text{int}} = 198$ nb^{-1}.

After the selection process just described, 1254 events are selected, 757 with positively charged muons and 497 with negative charge. Several sources of background events are identified at this stage. The QCD background mostly contains muons that come from the decay of b-hadrons, with a smaller contribution of muons from long-lived meson decays (mostly charged pions and kaons). Their contribution at high M_T is small. Electroweak processes other than the one under study also contribute: these are mainly $Z \to \mu^+\mu^-$ events where one of the muons lies beyond the detector acceptance ($|\eta| < 2.4$), thus escaping detection ($\sim$ 3% back-

ground). Muons from $Z \to \tau^+\tau^-$ and $W \to \tau\nu$ events, with the tau decaying into a muon, will have in general a lower momentum, and are strongly reduced by the selection cuts ($\sim 2\%$ contamination). The $t\bar{t}$ background is negligible (0.3%).

The $W \to \mu\nu$ signal yield is extracted from a binned likelihood fit to the observed M_T distribution. Given the limited event sample, the shapes of the different signal and background components are taken from Monte Carlo predictions, with the exception of the QCD background contribution, which is estimated using a data-driven method. Monte Carlo predictions are corrected for remaining differences with respect to data via efficiency correction factors. These factors are determined from tag-and-probe studies in $Z \to \mu^+\mu^-$ and dedicated studies as a function of the muon pseudo-rapidity. These studies are summarized in Section 5. The trigger correction factor amounts to (0.98 ± 0.03) when averaged over the W acceptance. The remaining efficiency correction factors (reconstruction and muon identification, isolation) are found to be more consistent with unity. The statistical precision of the studies in data is propagated as a systematic uncertainty on the measurement.

The fit provides as output parameters the normalization of QCD events and the $W \to \mu\nu$ yield. The M_T distribution is taken as the sum of three different contributions, each of them accounting for the different origin of the events: $W \to \mu\nu$ signal, QCD background and EWK backgrounds (Drell-Yan, $W \to \tau\nu$, $Z \to \tau^+\tau^-$ and $t\bar{t}$). EWK backgrounds are normalized to the $W \to \mu\nu$ yield on the basis of Monte Carlo event samples and known cross sections.

A high purity QCD template is obtained by using the same cuts as in the signal selection but the isolation cut, which is chosen as: $I^{\text{rel}}_{\text{comb}} > 0.20$. This data-based template used in the fits is shown in Fig. 2, compared with the Monte Carlo expectations for inverted ($I^{\text{rel}}_{\text{comb}} > 0.20$) and non-inverted ($I^{\text{rel}}_{\text{comb}} < 0.15$) samples. Conservatively, we use the full difference between these two Monte Carlo templates as an estimate of the systematic uncertainty on the QCD shape.

Estimated uncertainties on the scale and resolution of the muon momentum, as well as the intrinsic $\not{E}_T$ response from tracking and calorimetry (see Section 10) are propagated as systematic uncertainties to the signal shape, which is based on Monte Carlo. They are summarized in Section 10.

Figure 3 shows the fit to the observed M_T spectrum, together with the different templates used and the obtained yield. The measured yield can be interpreted as a cross section measurement for $\mathcal{L} = 198\,\text{nb}^{-1}$: $\sigma(pp \to W + X) \times BF(W \to \mu\nu) = 9.1 \pm 0.3$ (stat.) nb. Figure 4 shows the fits to the M_T distributions of positively and negatively charged W candidates, separately. The measured yields correspond to cross sections of $\sigma(pp \to W^+ + X \to \mu^+\nu + X) = 5.8 \pm 0.3$ (stat.) nb and $\sigma(pp \to W^- + X \to \mu^-\bar{\nu} + X) = 3.4 \pm 0.2$ (stat.) nb, respectively. The signal yield ratio is 1.69 ± 0.12 (stat.).

4 Extraction of the $Z \to \mu^+\mu^-$ signal yield

$Z \to \mu^+\mu^-$ events are characterized by the presence of two high-p_T isolated muons forming a di-muon system with high reconstructed invariant mass, consistent with the Z boson mass. The present analysis, due to the limited event sample available, is based on a cut-and-count strategy. The expected background is very low, and therefore it is estimated from Monte Carlo.

We select events in which one of the muons satisfies the same criteria described in Section 2 and used in the $W \to \mu\nu$ selection. Looser quality criteria are applied to the second muon in the event, namely a minimum number of 10 tracker hits in order to ensure a sensible measurement of the invariant mass of the pair. For each event, we consider all the possible di-muon pairs

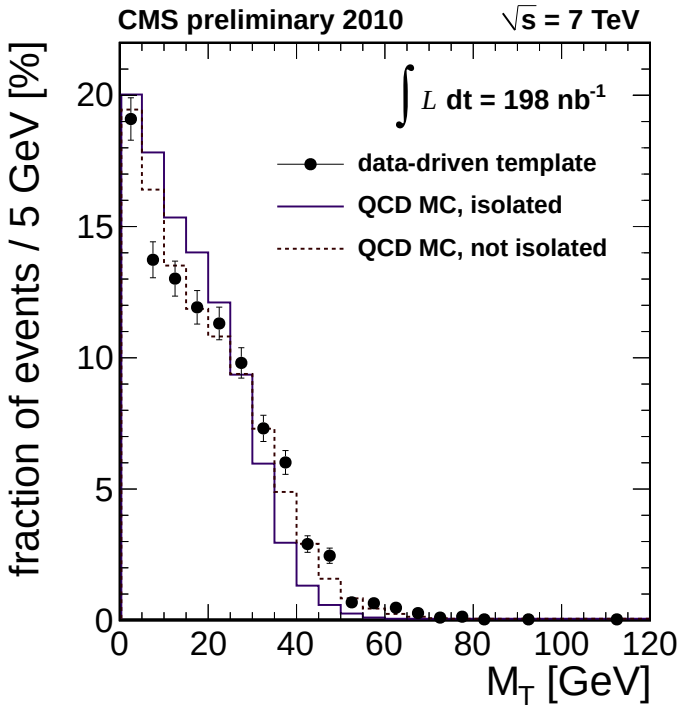

Figure 2: Comparison of the M_T distribution of QCD background in $W \to \mu\nu$ candidates, as derived from isolation inversion in data (points), with the same distribution expected from the simulation (dashed histogram). The Monte Carlo distribution predicted for the selected QCD sample (solid histogram), used to conservatively assign systematic uncertainties, is also shown for comparison.

made by opposite-charge muons with $p_T(\mu) > 20$ GeV/c with an invariant mass in the range $60 < m_{\mu\mu} < 120\,\text{GeV}/c^2$. One of the two muons must have $|\eta| < 2.1$, and be matched with a muon satisfying trigger criteria. The other muon must be in the region $|\eta| < 2.4$. Both muon candidates must be isolated according to the isolation variable $I_{\text{trk}} = \sum p_T(tracks)$, where $\sum p_T(tracks)$ is defined in Eq. 1. We require $I_{\text{trk}} < 3$ GeV/c for both muons.

We have analyzed a data sample of 198 nb^{-1} and 77 events pass the $Z \to \mu^+\mu^-$ event selection, which corresponds to a measurement: $\sigma(\text{pp} \to Z(\gamma^*) + X \to \mu^+\mu^- + X) = 0.42 \pm 0.05$ nb in the $[60, 120]$ GeV/c^2 di-muon mass range, within the applied kinematic cuts, where the quoted uncertainty is statistical. The acceptance of all previous cuts for the pseudo-rapidity and invariant mass ranges covered in the analysis is 47.6 ± 0.2 (stat.)%, as estimated from Monte Carlo simulations. The di-muon invariant mass of the selected Z candidates is shown in Figure 5. Data are compared with the Monte Carlo NLO expectations for this luminosity. The background, dominated by QCD, $t\bar{t}$ and $Z \to \tau^+\tau^-$ events, is negligible ($\sim 0.3\%$).

5 Muon efficiency studies in data

Muon reconstruction and identification, trigger and isolation efficiencies are initially estimated using Monte Carlo. We carry out several data-driven studies in order to estimate their accuracy and to apply corrections if necessary. The corrections are propagated into the Monte Carlo predictions for the analysis in Sections 3-4. The accuracy of these tests is propagated as systematics in the measurements, summarized in Section 10.

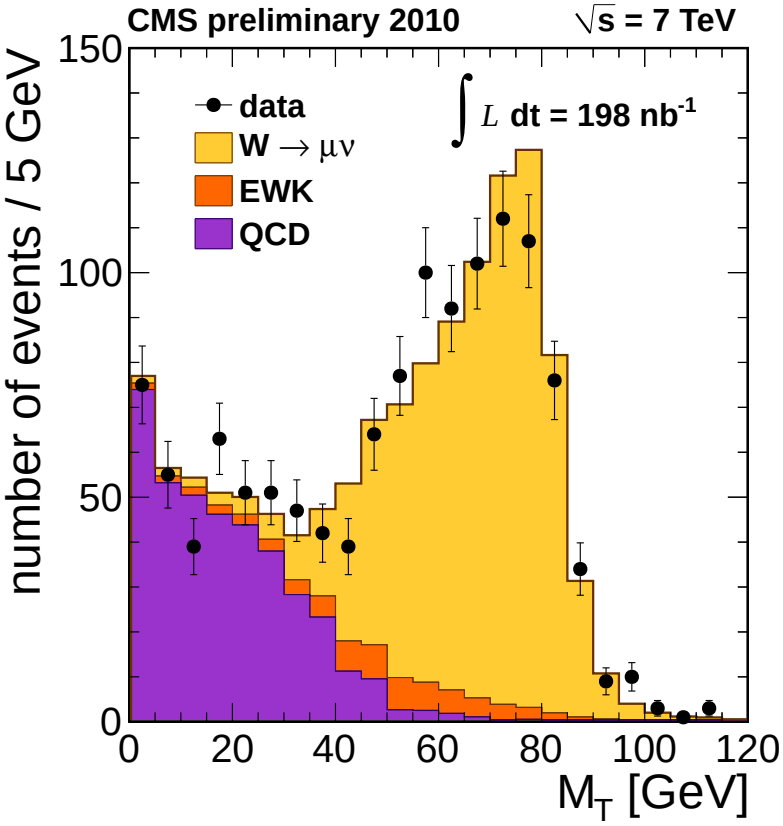

Figure 3: Fit to the M_T spectrum of W candidates (black points) together with the templates for the different processes, for an integrated luminosity of 198 nb^{-1}: W signal, other electroweak processes, and QCD background (solid histograms). The signal yield is $N_W = 818 \pm 27$, where the indicated error is statistical only.

The overall efficiency from muon reconstruction methods and identification criteria is studied with high-p_T inclusive muons ($p_T > 15\,\text{GeV}/c$) satisfying most of the selection criteria described in Section 2. This muon sample has a large b-decay component, resembling the prompt muons expected in W and Z production. Differences in efficiency between data and Monte Carlo are therefore interpreted as potential biases in the efficiency of our electroweak selected samples. The muon efficiency has three distinguishable components: 1) the efficiency to find a track in the inner tracker, 2) the efficiency to find a track in the muon chambers, 3) the efficiency of the remaining set of identification cuts. The inner tracker efficiency is studied using well-reconstructed tracks in the muon chamber as probes. The tracker efficiency in the muon chambers is probed with "tracker muons", which are tracks with loose matchings to muon segments, but not a muon track. Finally the efficiency of the remaining identification cuts is studied by switching them on and off and comparing the variations in efficiency observed in data and Monte Carlo. All checks provide results that are consistent with the Monte Carlo predictions within the statistical uncertainty of the checks, almost independently of the pseudo-rapidity region. The results are also compatible with dedicated tag-and-probe checks on the $Z \to \mu^+\mu^-$ sample. This statistical uncertainty, 3%, is propagated into the W measurement as a systematic uncertainty. In the Z case this uncertainty is found to be lower, 2.5%, due to the looser requirements on one of the muons in the event.

Trigger efficiencies are studied using $Z \to \mu^+\mu^-$ events. For the $W \to \mu\nu$ case we select $Z \to$

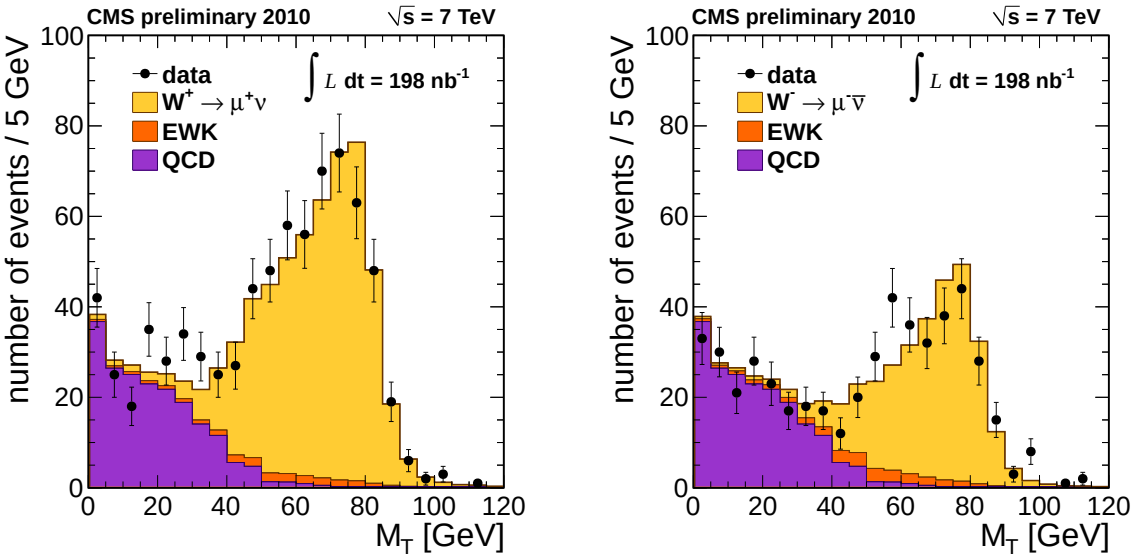

Figure 4: Fits to the M_T spectrum of positive and negative W candidates (black points) together with the templates for the different processes, for an integrated luminosity of 198 nb^{-1}: W signal, other electroweak processes, and QCD background (solid histograms). The signal yields are $N_{W^+} = 529 \pm 24$ and $N_{W^-} = 289 \pm 13$, where the indicated errors are statistical only.

$\mu^+\mu^-$ events requiring the same muon identification and isolation criteria used in the $W \to \mu\nu$ analysis. We split this sample in events in which both muons or only one of the two muons satisfy the requirements of the single-muon trigger. From the ratio of those two numbers we determine the trigger efficiency to be $(92 \pm 3)\%$, which is compatible with the Monte Carlo expectation, and gives a correction factor of $(98 \pm 3)\%$. Alternatively the trigger efficiency has been studied on high-p_T muons selected using jet $\not{E}_T$ and tau triggers. These triggers have been relatively stable over the initial data-taking period. They are relatively efficient selecting events with high-p_T muons, and about 20% of the $W \to \mu\nu$ events are selected by them. On this sample we apply all $W \to \mu\nu$ selection criteria but the isolation cut, relaxing the muon p_T cut to 15 GeV. Results are consistent with the ones determined from $Z \to \mu^+\mu^-$ events, within statistical and systematic uncertainties.

Finally, isolation efficiencies are estimated using a random cone technique. The essence of the method consists of "throwing" pre-defined directions in high-purity $W \to \mu\nu$, $Z \to \mu^+\mu^-$ events. These directions are defined by the direction (η,ϕ) of muons from a Monte Carlo sample. Muon directions in the original data event are not considered. Monte Carlo simulations show that the method provides unbiased estimates to a high level of accuracy ($\sim$ 0.5%). Figure 6 shows the final correction factors to be applied to the single-muon isolation efficiency estimated from Monte Carlo. The results confirm the Monte Carlo predictions the $W \to \mu\nu$ and $Z \to \mu^+\mu^-$ isolation criteria used in the analysis within the expected uncertainty of the method. No correction is applied to the simulation, and the observed deviations are propagated as systematic uncertainties.

6 Electron identification and selection

Electrons are identified in the CMS detector as clusters of ECAL energy deposits matched to tracks from the silicon tracker. The ECAL uses 75848 lead tungstate ($PbWO_4$) crystals with coverage in pseudorapidity up to $|\eta| < 1.5$ in a cylindrical barrel region (EB) and from $1.5 <$

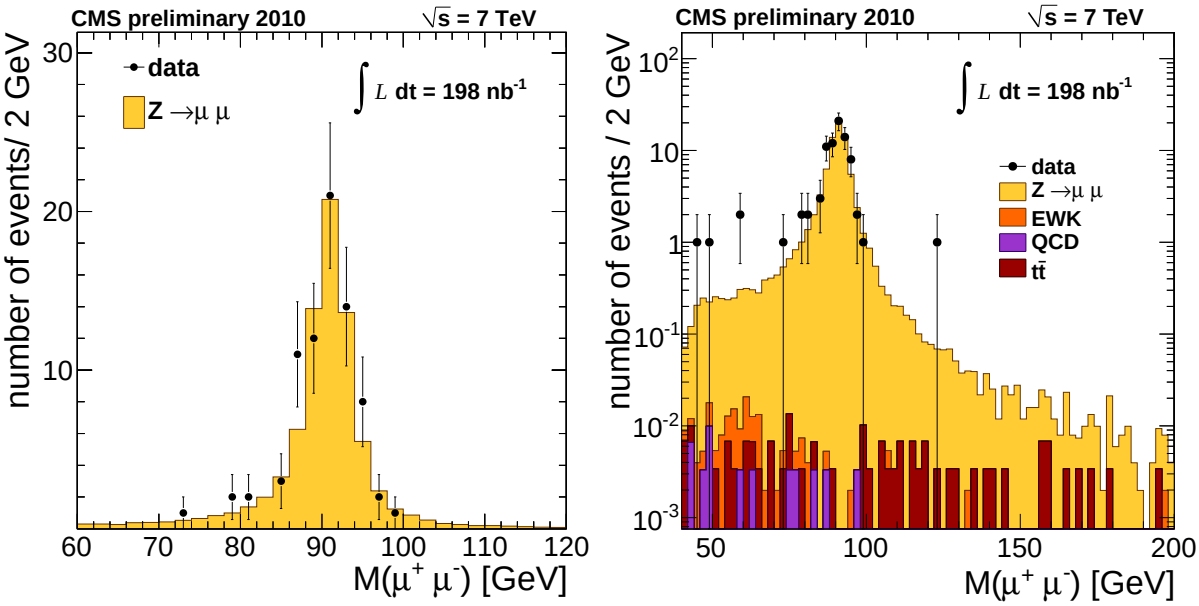

Figure 5: Invariant mass distribution of the selected $Z \to \mu^+\mu^-$ candidates in data superimposed to the MC expectation. Left: linear, right: logarithmic scale.

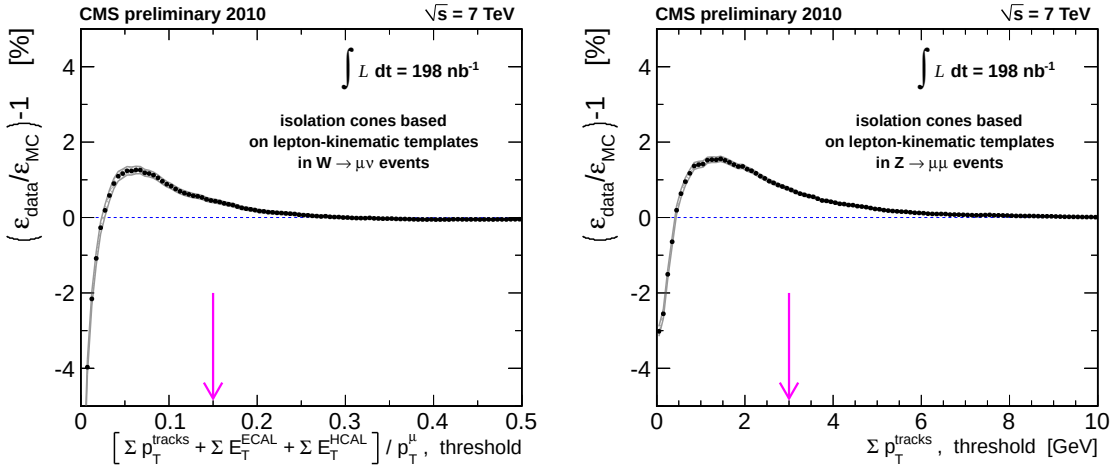

Figure 6: Isolation cut efficiency correction for prompt muons (per muon) as a function of the cut. Left: $W \to \mu\nu$ case, where the nominal cut is at 0.15. Right: $Z \to \mu^+\mu^-$ case, where the nominal cut is at 3 GeV.

$|\eta| < 3.0$ in two endcap regions (EE).

Electron candidates are selected online from events that: pass a "Level 1" (L1) trigger filter, evaluated by customized hardware, which requires a coarse-granularity region of the ECAL to have $E_T > 5$ GeV; and that subsequently pass a "High Level Trigger" (HLT) software filter, requiring an ECAL cluster with $E_T > 15$ GeV, using the full granularity of the ECAL and E_T measurements calibrated to offline precision [19].

Electron candidates require an ECAL cluster [20] with $E_T > 20$ GeV for W or Z candidates, and with $|\eta| < 1.4442$ for EB clusters or $1.566 < |\eta| < 2.500$ for EE clusters. ECAL clusters are required to match tracks using an algorithm [21] which accounts for possible energy loss due

to bremsstrahlung in the tracker layers. Particles misidentified as electrons are suppressed by: requiring the track trajectory η and ϕ, extrapolated to the ECAL, to match the ECAL cluster η and ϕ; by limiting the amount of HCAL energy measured in a cone of $\Delta R < 0.15$ around the ECAL cluster direction; and by requiring a narrow ECAL cluster width in η.

Electrons from photon conversions are reduced by requiring that the electron track has no missing tracker hits before the first hit in the reconstructed track assigned to the electron. If a partner track is found with an $x - y$ distance to the electron track when both are parallel less than 0.02 cm, and forming a small opening angle with the electron track, the candidate is also rejected as a conversion.

Misidentified particles, as well as real electrons arising from jet fragmentation, are suppressed by imposing limits on the additional sums of HCAL E_T, ECAL E_T, and track p_T in a cone of $\Delta R < 0.3$ around the electron candidate direction (isolation). Tracks and ECAL energy associated with the electron are excluded from these sums. Limits range from 3–10% of the electron candidate E_T, depending on the subdetector and ECAL region.

Using these criteria, two cut-based electron selection algorithms are adopted, based on simulation studies which optimize signal and background levels: a tight algorithm with 75% efficiency for W electron selection, and a looser algorithm with 90% efficiency for Z electron selection.

7 Measurement of the $W \to e\nu$ signal yield

W candidates are required to have one electron, with ECAL cluster $E_T > 20$ GeV, satisfying the criteria of the previous section. If a second electron candidate is found, satisfying looser criteria and with $E_T > 20$ GeV, the event is rejected as a Z candidate. This selection results in 1931 candidate events in 198 nb^{-1}.

Remaining backgrounds consist of QCD di-jet events, prompt high-E_T photons, Z events, and $W \to \tau\nu$ events. The first two sources are characterized by small intrinsic $\not{E}_T$, and can be separated from $W \to e\nu$ signal from an analysis of the $\not{E}_T$ distribution. The last two sources can be modeled successfully by Monte Carlo simulation.

The $W \to e\nu$ signal is extracted via an unbinned maximum likelihood fit to the $\not{E}_T$ distribution. $W \to e\nu$ signal and electroweak background distributions are derived from simulation. The QCD background is described well by a modified Rayleigh distribution, $x \exp(-x^2/2(\sigma_0 + \sigma_1 x)^2)$, where the resolution term $\sigma_0 + \sigma_1 x$ is allowed to be linearly $\not{E}_T$-dependent. The free parameters of the fit are the QCD background yield N_{QCD}, the W signal yield N_W, and the Rayleigh shape parameter σ_0. The $\not{E}_T$-dependent term σ_1 is fixed from simulation to be 0.14/GeV. Figure 7 shows the $\not{E}_T$ distribution of $W \to e\nu$ candidates and the results of the likelihood fit. The fit describes the data well, with a p-value of 31% for the Kolmogorov-Smirnov test score. The $W \to e\nu$ signal yield estimated from the fit is 799.7 ± 30.6 events.

For $W^+ \to e^+\nu$ and $W^- \to e^-\overline{\nu}$ channels, the signal is extracted via a simultaneous unbinned maximum likelihood fit to the separate $\not{E}_T$ distributions of $W^+ \to e^+\nu$ and $W^- \to e^-\overline{\nu}$ candidates. The PDFs and free parameters of the fit are identical to that of the charge-inclusive fit, except that the QCD background shape parameter σ_0 is constrained to be the same for both samples. Figure 8 shows the $\not{E}_T$ distribution of $W^+ \to e^+\nu$ and $W^- \to e^-\overline{\nu}$ candidates and the results of the likelihood fit. The signal yields are 457.5 ± 22.9 for $W^+ \to e^+\nu$ and 338.8 ± 19.8 for $W^- \to e^-\overline{\nu}$, with a correlation coefficient of +0.016. The resulting signal yield ratio is 1.35 ± 0.10.

The sources of systematic uncertainty for the fit procedure are: the uncertainty in the relative normalization of the electroweak background component, shape biases in the QCD background, and shape biases in the signal component. The electroweak background normalization has uncertainty primarily due to any potential mis-modeling of the acceptance and efficiency of electrons from $W \to \tau\nu$ and $Z \to e^+e^-$ relative to that of $W \to e\nu$, resulting in systematic biases of 0.1%. The QCD background shape biases are estimated by examining the $\not\!\!E_T$ distributions of events passing the $W \to e\nu$ selection with electron selection criteria inverted, such as isolation (see Fig. 9), and $\eta - \phi$ matching requirements between the electron track and its ECAL cluster. The functional form chosen describes all of these samples well, and with the same parameter values. The fit is also performed with σ_1 allowed to float. The systematic bias in the signal yield, resulting from these alternative parameter values, is 2.2%. Uncertainties from signal shape biases are estimated by the mean expected bias from alternative $\not\!\!E_T$ shapes. The alternative shapes span the range of $\not\!\!E_T$ shapes obtained from varying the electron energy scale by $\pm 1\%$ in EB and $\pm 3\%$ in EE. This variation of scale can change the signal yield by up to 2.7%. The alternative shapes also span the range of W $\not\!\!E_T$ recoil allowed by using the minimum bias data to constrain the underlying event energy modelling in our W simulation. The resulting mean bias in the signal yield expected from this range is 1.4%. The $\not\!\!E_T$ shape will also vary due to the uncertainty of efficiency corrections to the simulation (as described in Section 9); this translates into signal yield variations of up to 0.3%.

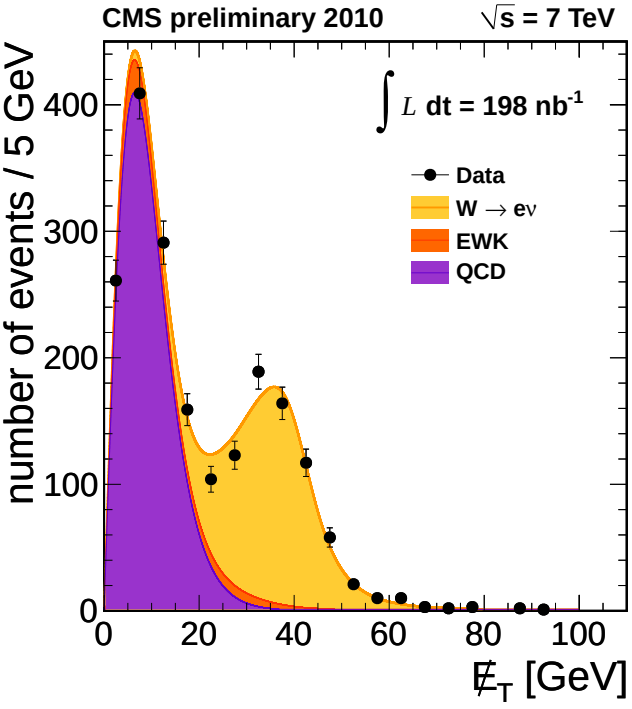

Figure 7: Distribution of $\not\!\!E_T$ for the selected $W \to e\nu$ candidates in data (points). Superimposed are the results of the likelihood fit for QCD background (violet), all backgrounds (orange), and signal plus background (yellow).

8 Measurement of the $Z \to e^+e^-$ signal yield

Z candidates are required to have two electrons, with ECAL cluster $E_T > 20$ GeV, satisfying the criteria of the Section 6, but with a looser operating point than the W selection for electrons.

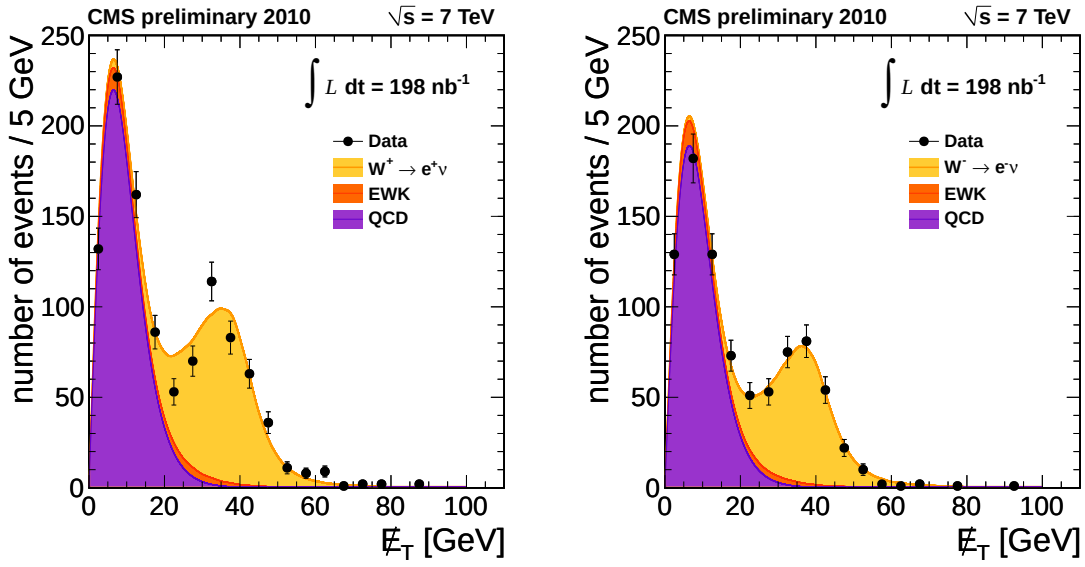

Figure 8: Distribution of $\not\!\!E_T$ for the selected $W^+ \to e^+\nu$ candidates (left) and $W^- \to e^-\overline{\nu}$ candidates (right) in data (points). Superimposed are the results of a simultaneous likelihood fit for QCD background (violet), all backgrounds (orange), and signals plus background (yellow).

The invariant mass of the electron pair is required to be between 60 and 120 GeV. This selection results in 61 candidate events in 198 nb^{-1}. Simulations of QCD di-jets estimate a background of much less than one event. Figure 10 shows the mass distribution of $Z \to e^+e^-$ candidates, with predictions from simulation superimposed. The data exhibit an energy scale shift relative to simulation of -1%; such a shift is well-covered by the systematic uncertainties assigned to electron energy scale in the results presented here.

9 Electron efficiency studies in data

Electron reconstruction, identification, isolation and trigger efficiencies are estimated using Monte Carlo. Cross checks were carried out in order to identify possible disagreements between data and simulation and apply corrections if necessary.

Electron reconstruction efficiency is estimated from a sample of Z candidates, where one electron has tight identification and isolation requirements, and the other electron is an ECAL cluster, which passes loose shower shape and isolation requirements (which are expected from simulations to be uncorrelated with reconstruction efficiency). Estimated QCD backgrounds for this sample are less than 1%. The measured efficiency is the fraction of probes reconstructed as electrons. The reconstruction efficiency for the EB is $99.3 \pm 1.4\%$ to be compared with the simulation prediction 98.5 %, resulting in a ratio of $100.8 \pm 1.4\%$. For EE electrons, an efficiency of $96.8 \pm 3.4\%$ is observed where 96.1% is expected, resulting in a correction of $100.8 \pm 3.5\%$. The simulated W and Z signal efficiencies are scaled by these ratios to reflect the measured efficiencies.

The efficiency of electron identification, isolation, and conversion rejection requirements is estimated by a similar technique. Z candidates are selected for which one electron candidate has tight requirements and the other is a reconstructed electron with isolation (identification and conversion) requirements applied to provide unbiased electrons for testing the identification and conversion (isolation) efficiency with background content less than 0.5% (2%) for the W (Z) selection. The total efficiency of these selection steps for the EB W candidates is $77.5 \pm 4.7\%$, to

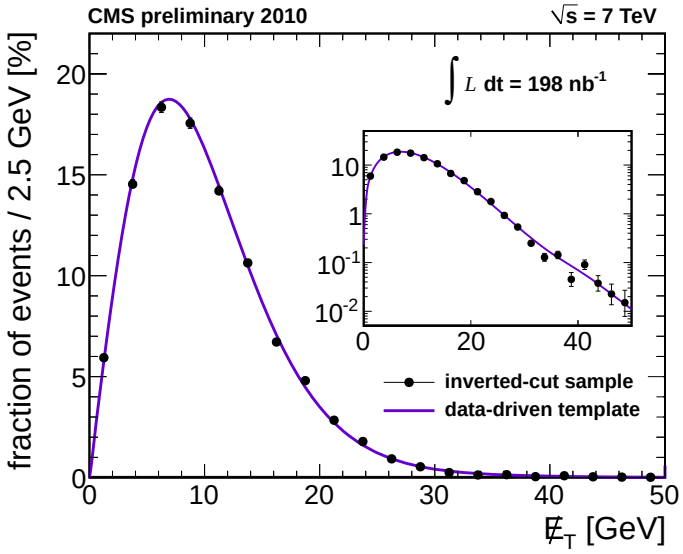

Figure 9: Distribution of $\not\!\!E_T$ for a background-dominated sample of events in the data failing the cluster/track matching requirements of the $W \to e\nu$ candidate selection, with only ECAL isolation applied (points). The result of the fit (superimposed in dark blue) is used to fix the parameter σ_1 of the QCD background shape.

be compared with the simulation prediction 85.1 %, resulting in a ratio of $91.1 \pm 5.5\%$. For the EE W selection, an efficiency of $75.1 \pm 8.6\%$ is observed where 76.2% is expected, resulting in a correction of $98.6 \pm 11.3\%$. The simulated W and Z electron efficiencies are scaled by these ratios to reflect the measured efficiencies. The corresponding ratios for the EB and EE Z electron selection are $97.0 \pm 3.4\%$ and $93.0 \pm 7.2\%$, respectively. The efficiency of electron isolation requirements can also be estimated using the random cones technique described in Section 5. The results confirm the MC predictions within 1.8% (1.4%), for both EB (EE) electrons, where the uncertainty is dominated by biases in the random cone method due to leakage of electron energy into the isolation cone.

The efficiency of the L1 and HLT online selection was estimated from samples of minimum bias collisions (selected with scintillation counters) along with samples from an HLT algorithm which has minimum bias requirements at L1 and a complete emulation of the offline ECAL cluster reconstruction in the HLT. All of the W candidates in these samples pass the W online selection, with a 68 %CL lower bound on the efficiency of 99.2% for EB and 98.9% for EE.

The product of all of the efficiency ratios for all selection steps is $93.4 \pm 6.0\%$ ($102.6 \pm 12.0\%$) for EB (EE) W electron selection; the corresponding results for Z electron selection are $97.8 \pm 3.8\%$ ($93.5 \pm 8.2\%$) for EB (EE). For $W \to e\nu$ signal, these corrections result in an overall signal efficiency of $75.7 \pm 4.6\%$. For $W^+ \to e^+\nu$ and $W^- \to e^-\overline{\nu}$, the efficiencies are $75.4 \pm 4.6\%$ and 76.1 ± 4.6, respectively. For $Z \to e^+e^-$, the corrected total signal selection efficiency is $80.0 \pm 5.8\%$. Studies of electron candidates identified as photon conversions (but otherwise passing other selection requirements) indicate that the W and Z selection are charge symmetric at the level of 3%. This uncertainty is added to results for the $W^\pm$ cross sections as well as their ratio.

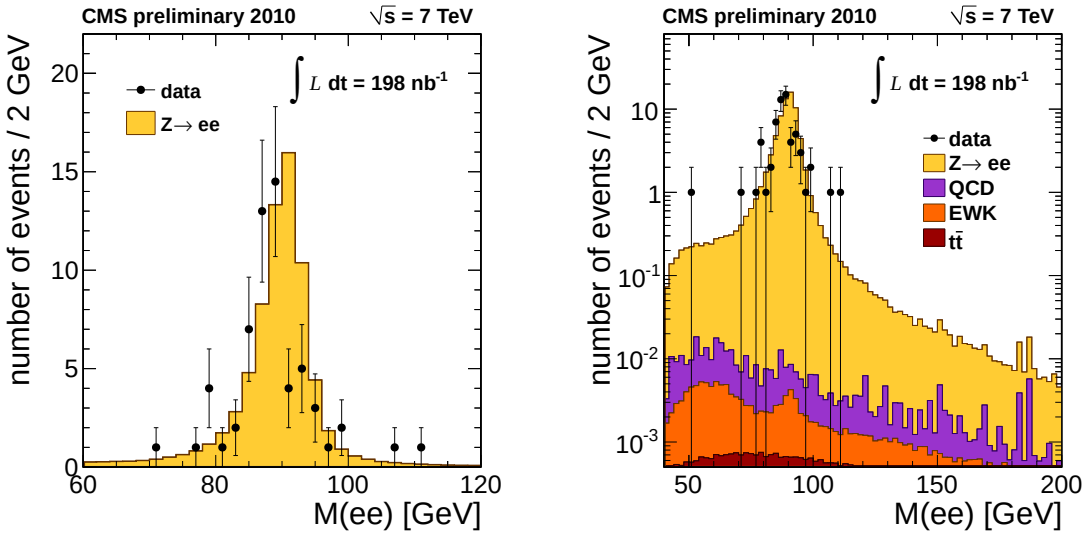

Figure 10: Distribution of M_{ee} for the selected $Z \to e^+e^-$ candidates in data (points). Superimposed are simulated estimates of signal and background components, normalized to 198 nb^{-1}.

10 Systematic uncertainties

The largest uncertainty for the cross section measurement comes from the luminosity measurement, currently estimated to be 11% [10]. This uncertainty should decrease in the future. We quote it separately from the other systematic uncertainties.

The first group of sources of systematics is related with uncertainties in the experimental response predicted by CMS simulations. Particularly important are estimates of lepton reconstruction, identification, trigger and isolation efficiencies, which are discussed in Sections 5 and 9.

Sub-dominant systematic uncertainties come from the lepton energy/momentum scale and resolution. Studies of high-energy cosmic ray events, alignment discrepancies between inner tracker extrapolations and muon chamber positions, low-mass dimuon resonances and estimated uncertainties on tracker alignment show that scale shifts above 1% for muons with $p_T \sim 40\,\mathrm{GeV}/c$ can be excluded. This leads to a small uncertainty in the $W \to \mu\nu$ analysis, 1%. In the electron case, scale shifts as large as 3% cannot be ignored, leading to a systematic uncertainty in the $W \to e\nu$ cross section of 2.7%.

The last source of experimental uncertainty is the limited knowledge of the intrinsic hadronic recoil response which contributes to the $\not{E}_T$ measurement. Studies of photon plus jet final states [12] and the recoil distribution against leptons in W events indicate that discrepancies as large as 10% between data and Monte Carlo for the response in this relatively low-$\not{E}_T$ region cannot be excluded. This uncertainty has a relatively small impact on $W \to \mu\nu$, and a 1.4% impact on the $W \to e\nu$ cross section.

The QCD background shapes are fitted in the signal extraction procedure, and studies with Monte Carlo show that possible biases are small compared with the statistical precision of the measurement. Since the contributions from the electroweak backgrounds is fixed as a relative contribution to the $W \to \ell\nu$ signal component, theoretical biases in their normalization can be neglected.

Theoretical uncertainties in the $W \to \ell\nu$ cross section measurement enter in the determination

of the acceptance of the detector and selection cuts. The Monte Carlo estimates are based on simulations that use a NLO generator (POWHEG) as input. Events are re-weighted according to different PDF set assumptions (CTEQ6.6 [22], MSTW08NLO [2], NNPDF2.0 [23]). The observed variations in the acceptance are $\lesssim$ 2%. Remaining theoretical uncertainties due the treatment of initial-state radiation, final-state QED radiation, missing electroweak effects of renormalization/factorization scale assumptions amount to $\sim$ 1.5%.

Table 2 and 3 shows the the systematic uncertainties in the W and Z cross section measurement for muons and electron channels, respectively. The main uncertainties are statistical in nature, and will decrease as more data is collected and analyzed.

Table 2: Table of systematic uncertainties for the muon channels. Dashed entries are either not applicable to the channel or negligible.

Source	W channel (%)	Z channel (%)
Muon reconstruction/identification	3.0	2.5
Trigger efficiency	3.2	0.7
Isolation efficiency	0.5	1.0
Muon momentum scale/resolution	1.0	0.5
$\not{E}_{\mathrm{T}}$ scale/resolution	1.0	-
Background subtraction	3.5	-
PDF uncertainty in acceptance	2.0	2.0
Other theoretical uncertainties	1.4	1.6
TOTAL (without luminosity uncertainty)	6.3	3.8
Luminosity	11.0	11.0

Table 3: Table of systematic uncertainties for the electron channels. Dashed entries are either not applicable to the channel or negligible.

Source	W channel (%)	Z channel (%)
Electron reconstruction/identification	6.1	7.2
Trigger efficiency	0.6	-
Isolation efficiency	1.1	1.2
Electron momentum scale/resolution	2.7	-
$\not{E}_{\mathrm{T}}$ scale/resolution	1.4	-
Background subtraction	2.2	-
PDF uncertainty in acceptance	2.0	2.0
Other theoretical uncertainties	1.3	1.3
TOTAL (without luminosity uncertainty)	7.7	7.7
Luminosity	11.0	11.0

11 Results

11.1 Cross Sections

For an integrated luminosity of 198 nb^{-1} we measure the following total cross sections for W production:

$$\begin{aligned}
\sigma(\text{pp} \to \text{W} + X \to \mu\nu + X) &= 9.14 \pm 0.33(\text{stat.}) \pm 0.58(\text{syst.}) \pm 1.00(\text{lumi.})\ \text{nb}, \\
\sigma(\text{pp} \to \text{W} + X \to \text{e}\nu + X) &= 9.34 \pm 0.36(\text{stat.}) \pm 0.70(\text{syst.}) \pm 1.03(\text{lumi.})\ \text{nb}, \\
\sigma(\text{pp} \to \text{W} + X \to \ell\nu + X) &= 9.22 \pm 0.24(\text{stat.}) \pm 0.47(\text{syst.}) \pm 1.01(\text{lumi.})\ \text{nb}.
\end{aligned}$$

The NNLO prediction (computed with FEWZ [24, 25]) with MSTW 2008 PDF is 10.44 ± 0.52 nb, which agrees well with this result.

The results for charged W production are given by:

$$\begin{aligned}
\sigma(\text{pp} \to \text{W}^+ + X \to \mu^+\nu + X) &= 5.75 \pm 0.26(\text{stat.}) \pm 0.36(\text{syst.}) \pm 0.63(\text{lumi.})\ \text{nb}, \\
\sigma(\text{pp} \to \text{W}^+ + X \to \text{e}^+\nu + X) &= 5.18 \pm 0.26(\text{stat.}) \pm 0.42(\text{syst.}) \pm 0.57(\text{lumi.})\ \text{nb}, \\
\sigma(\text{pp} \to \text{W}^+ + X \to \ell^+\nu + X) &= 5.50 \pm 0.18(\text{stat.}) \pm 0.29(\text{syst.}) \pm 0.61(\text{lumi.})\ \text{nb}.
\end{aligned}$$

$$\begin{aligned}
\sigma(\text{pp} \to \text{W}^- + X \to \mu^-\overline{\nu} + X) &= 3.39 \pm 0.15(\text{stat.}) \pm 0.21(\text{syst.}) \pm 0.37(\text{lumi.})\ \text{nb}, \\
\sigma(\text{pp} \to \text{W}^- + X \to \text{e}^-\overline{\nu} + X) &= 4.13 \pm 0.24(\text{stat.}) \pm 0.34(\text{syst.}) \pm 0.45(\text{lumi.})\ \text{nb}, \\
\sigma(\text{pp} \to \text{W}^- + X \to \ell^-\overline{\nu} + X) &= 3.60 \pm 0.13(\text{stat.}) \pm 0.19(\text{syst.}) \pm 0.40(\text{lumi.})\ \text{nb}.
\end{aligned}$$

Results are combined between lepton channels by maximizing a likelihood which accounts for the individual statistical and systematic uncertainties and their correlations. The NNLO predictions for these cross sections are 6.15 ± 0.29 nb for W^+ and 4.29 ± 0.23 nb for W^-. We also measure the following cross sections for Z production, using 198 nb^{-1}:

$$\begin{aligned}
\sigma(\text{pp} \to \text{Z}(\gamma^*) + X \to \mu^+\mu^- + X) &= 0.881^{+0.104}_{-0.097}(\text{stat.})^{+0.042}_{-0.034}(\text{syst.}) \pm 0.097(\text{lumi.})\ \text{nb}, \\
\sigma(\text{pp} \to \text{Z}(\gamma^*) + X \to \text{e}^+\text{e}^- + X) &= 0.884^{+0.118}_{-0.108}(\text{stat.})^{+0.076}_{-0.059}(\text{syst.}) \pm 0.097(\text{lumi.})\ \text{nb}, \\
\sigma(\text{pp} \to \text{Z}(\gamma^*) + X \to \ell^+\ell^- + X) &= 0.882^{+0.077}_{-0.073}(\text{stat.})^{+0.042}_{-0.036}(\text{syst.}) \pm 0.097(\text{lumi.})\ \text{nb}.
\end{aligned}$$

The reported $Z(\gamma^*)$ cross sections are limited to the di-lepton invariant mass range $[60, 120]$ GeV/c^2, and corrected for the kinematic acceptance. The NNLO prediction for Z production is 0.97 ± 0.04 nb, in good agreement with our measurements.

Figure 11 shows the CMS measurements together with measurements at lower-energy hadron colliders.

11.2 Cross Section Ratios

The ratio of cross sections for W and Z(γ^*) production is given by:

$$\frac{\sigma(\text{W})}{\sigma(\text{Z}(\gamma^*))} = \frac{N_\text{W}}{N_\text{Z}} \frac{\varepsilon_\text{Z}}{\varepsilon_\text{W}} \frac{A_\text{Z}}{A_\text{W}}\,.$$

The uncertainty from A_Z/A_W is determined from MC generator studies to be 2%. The two different decay channels are combined by assuming fully correlated uncertainty for the acceptance factor, with other uncertainties assumed uncorrelated. This results in the measurements:

$$\begin{aligned}
\sigma(\text{pp} \to \text{W} + X \to \mu\nu + X)/\sigma(\text{pp} \to \text{Z}(\gamma^*) + X \to \mu^+\mu^- + X) &= 10.38^{+1.34}_{-1.15}(\text{stat.})^{+0.78}_{-0.64}(\text{syst.})\,, \\
\sigma(\text{pp} \to \text{W} + X \to \text{e}\nu + X)/\sigma(\text{pp} \to \text{Z}(\gamma^*) + X \to \text{e}^+\text{e}^- + X) &= 10.57^{+1.54}_{-1.30}(\text{stat.})^{+1.20}_{-0.97}(\text{syst.})\,, \\
\sigma(\text{pp} \to \text{W} + X \to \ell\nu + X)/\sigma(\text{pp} \to \text{Z}(\gamma^*) + X \to \ell^+\ell^- + X) &= 10.46^{+0.99}_{-0.88}(\text{stat.})^{+0.65}_{-0.56}(\text{syst.})\,.
\end{aligned}$$

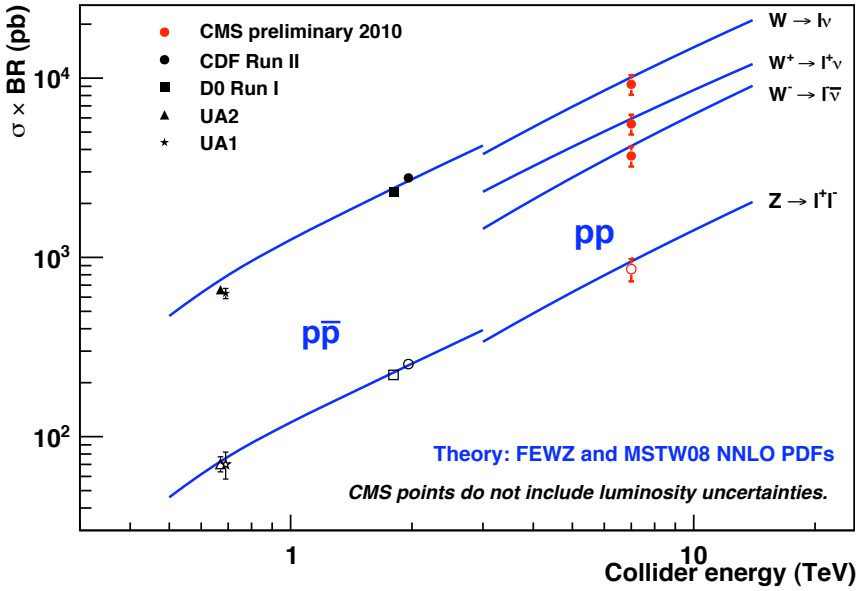

Figure 11: Measurements of inclusive cross sections from CMS and experiments at lower-energy colliders. The solid symbols represent $\sigma(\mathrm{W} \to \ell\nu) \times BF(\mathrm{W} \to \ell\nu)$ and the hollow symbols, $\sigma(\mathrm{Z}(\gamma^*) \to \ell^+\ell^-) \times BF(\mathrm{Z} \to \ell^+\ell^-)$.

The NNLO prediction for this ratio is 10.74 ± 0.04, in agreement with our measurement.

The cross section ratio of W^+ and W^- is given by

$$\frac{\sigma(\mathrm{W}^+)}{\sigma(\mathrm{W}^-)} = \frac{N_{\mathrm{W}^+}}{N_{\mathrm{W}^-}} \frac{\varepsilon_{\mathrm{W}^-}}{\varepsilon_{\mathrm{W}^+}} \frac{A_{\mathrm{W}^-}}{A_{\mathrm{W}^+}}$$

Results are combined between the charge and lepton channels by maximizing a likelihood which accounts for the individual statistical and systematic uncertainties and their correlations. The uncertainty from $\frac{A_{\mathrm{W}^-}}{A_{\mathrm{W}^+}}$ is determined from MC generator studies to be 2%. The two different decay channels are combined by assuming fully correlated uncertainty for the acceptance factor, with other uncertainties assumed uncorrelated. This results in the measurements:

$$\sigma(\mathrm{pp} \to \mathrm{W}^+ + X \to \mu^+\nu + X)/\sigma(\mathrm{pp} \to \mathrm{W}^- + X \to \mu^-\overline{\nu} + X) = 1.69 \pm 0.12(\mathrm{stat.}) \pm 0.04(\mathrm{syst.})\,,$$
$$\sigma(\mathrm{pp} \to \mathrm{W}^+ + X \to \mathrm{e}^+\nu + X)/\sigma(\mathrm{pp} \to \mathrm{W}^- + X \to \mathrm{e}^-\overline{\nu} + X) = 1.26^{+0.10}_{-0.09}(\mathrm{stat.}) \pm 0.05(\mathrm{syst.})\,,$$
$$\sigma(\mathrm{pp} \to \mathrm{W}^+ + X \to \ell^+\nu + X)/\sigma(\mathrm{pp} \to \mathrm{W}^- + X \to \ell^-\overline{\nu} + X) = 1.51^{+0.08}_{-0.07}(\mathrm{stat.}) \pm 0.04(\mathrm{syst.})\,.$$

The NNLO prediction is 1.43 ± 0.04. The combined result is in agreement with prediction, however the individual results each differ at the two sigma level.

12 Lepton charge asymmetry

W^+ and W^- bosons are produced at different rates in pp collisions, due to the prevalence of u quarks over d quarks. Precise information on the W charge asymmetry provides useful constraints on parton distribution functions (PDFs). Current theoretical predictions using up-to-date PDFs predict an asymmetry of approximately 0.2.

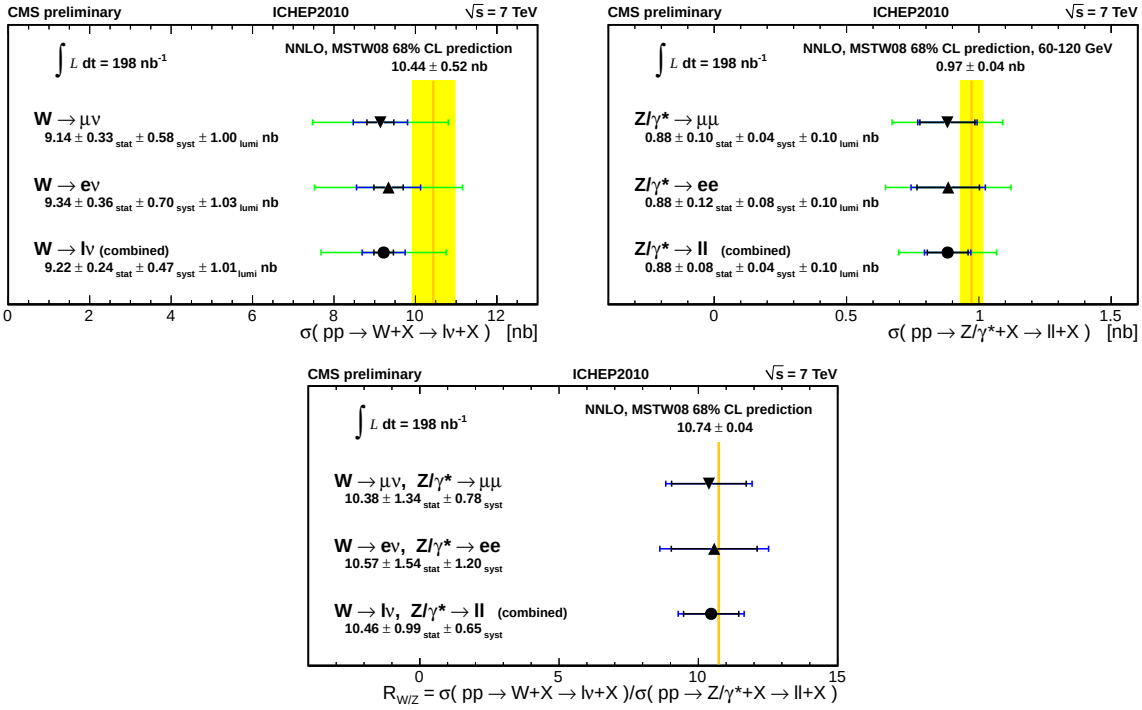

Figure 12: Summary of results for W and $Z(\gamma^*)$ production, and ratio.

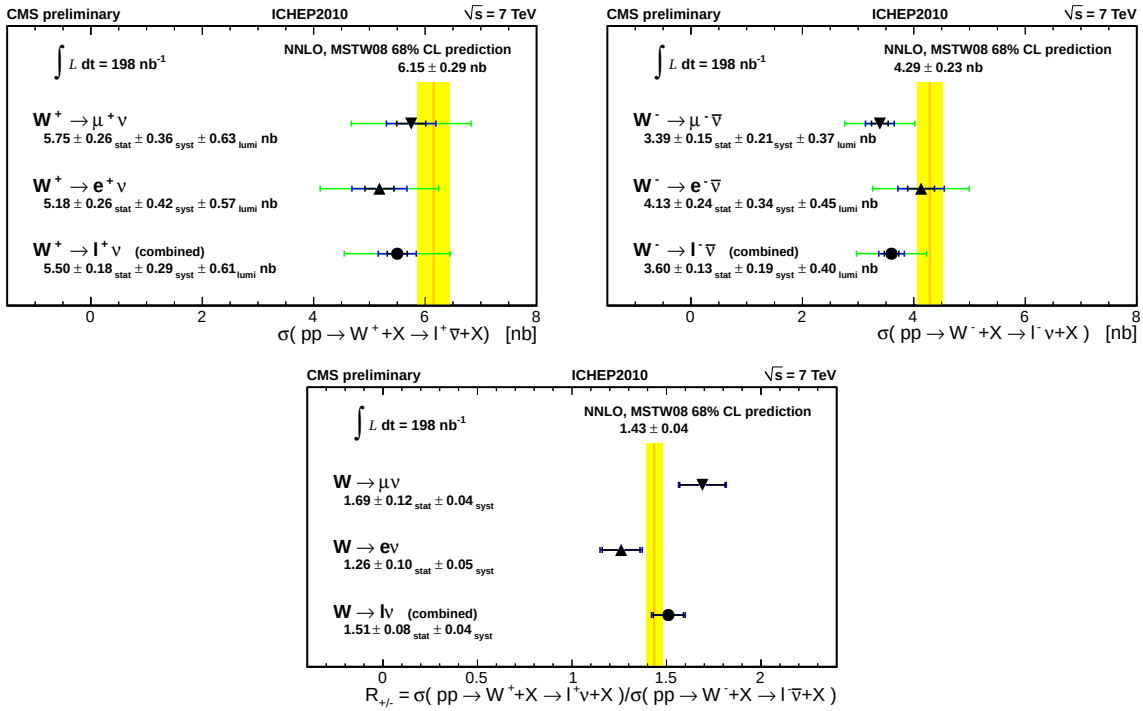

Figure 13: Summary of results for W^+ and W^- production, and ratio.

We present first measurements of the lepton charge asymmetry as a function of pseudorapidity in the inclusive process $pp \to W^{\pm} X \to \ell^{\pm} \nu X$, where ℓ stands for electrons and muons. The asymmetry is defined as follows:

$$A(\eta) = \frac{d\sigma^{(+)}/d\eta_\ell - d\sigma^{(-)}/d\eta_\ell}{d\sigma^{(+)}/d\eta_\ell + d\sigma^{(-)}/d\eta_\ell}, \tag{2}$$

where η_ℓ is the pseudorapidity of the charged lepton. Previous feasibility studies for the muon channel [26] indicate that a total error below 0.03 can be obtained with 10 pb^{-1}, dominated by the uncertainty on the ratio of efficiencies, to be compared to a variation of about 0.04 from different PDF sets.

The lepton reconstruction and the event selection are the same as in the measurements of the inclusive cross sections described above. The data sets used amount to 198 nb^{-1}.

The raw lepton charge asymmetry differs from the asymmetry for charged W bosons through the slightly different acceptances for positive and negative leptons. The ratio of efficiencies for reconstructing positive and negative leptons are consistent with one within statistical errors. Charge mis-assignment, well below 1%, is a negligible effect for the present analysis.

The numbers of positive and negative leptons is extracted in each of three bins of $|\eta|$, using a fit to the $\not\!\!E_T$ distribution for electrons, and M_T distribution for muons. The $\not\!\!E_T$ is obtained from the Particle Flow algorithm.

Figure 14 shows the raw lepton charge asymmetries. The ratio of acceptances, A^+/A^-, is needed in order to extract the $W^{\pm}$ asymmetries. This ratio is nearly the same for electrons and muons; any differences are much less than the current statistical errors. The theory curve was computed using the ResBos [27–32] program and the NNLO calculation by C. Anastasiou et al. [33], interfaced with the CTEQ6.6 PDF set.

13 Di-muon forward-backward asymmetry

The forward-backward asymmetry for lepton pairs, A_{FB}, depends on the electromagnetic and weak coupling constants for left-handed and right-handed charged leptons. It should be small for di-lepton invariant masses near the Z peak, and sizable for masses around 70 GeV and above 110 GeV. If a new neutral gauge boson is produced in addition to the photon and Z boson, A_{FB} will deviate from its Standard Model value.

This measurement is based on the di-muon sample. The selection of muons and events is the same as in the inclusive $Z \to \mu^+\mu^-$ cross section measurement, except for the cuts on the di-muon mass. Figure 15 shows the distributions of the di-muon transverse momentum (top left) and rapidity (top right), compared to the expectations from the full simulation. No discrepancies are observed.

The asymmetry is measured in the Collins-Soper frame [34] as a function of $\cos\theta^*_{CS}$, for three bins in mass. The distribution of $\cos\theta^*_{CS}$ for all masses is shown in Fig. 15, bottom left. Finally, A_{FB} is shown as a function of mass in Fig. 15, bottom right. This asymmetry has not been corrected for resolution or dilution effects. These effects are important in a precision measurement, but are small compared to the current statistical errors. The data agree with expectations within the statistical uncertainties.

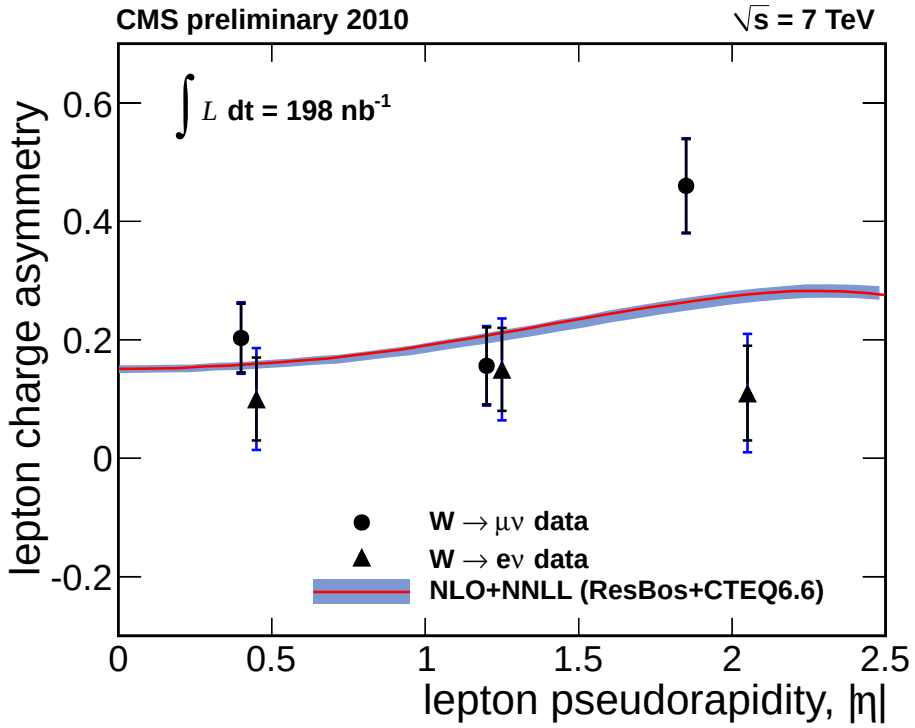

Figure 14: Raw lepton charge asymmetry in three bins of $|\eta|$. Electron and muon results are plotted together, and compared to the theoretical prediction. These results have not been corrected for relative differences in ℓ^+ and ℓ^- acceptance.

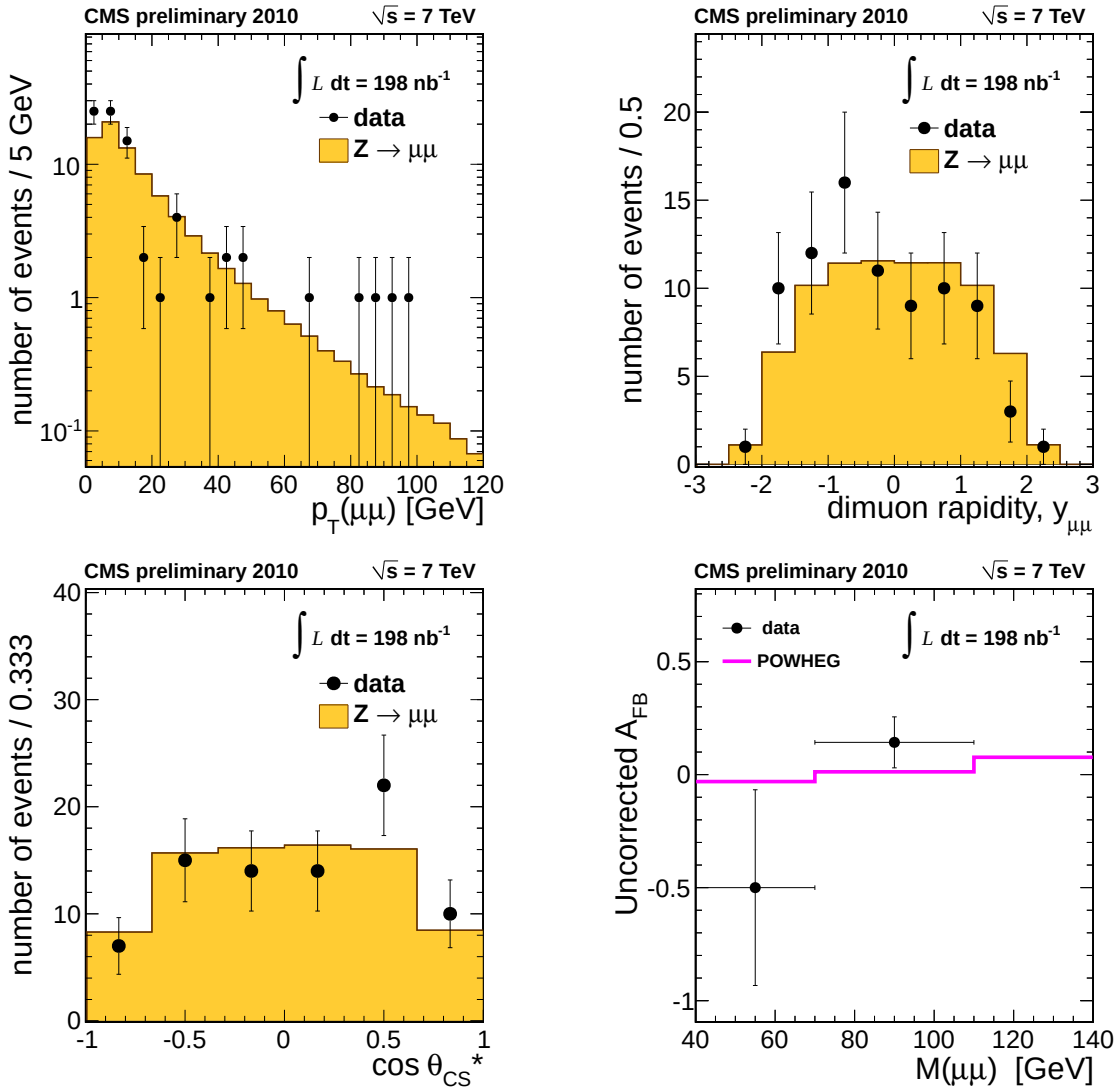

Figure 15: Di-muon kinematic distributions and asymmetry, comparing data to the simulation. Top left: di-muon transverse momentum. Top right: di-muon rapidity. Bottom left: $\cos\theta^*_{CS}$. Bottom right: A_{FB} for three bins in di-muon mass.

14 Associated production of hadronic jets

We study the production of hadronic jets along with W bosons reconstructed in leptonic decay modes. The lepton selections are identical to those described in Section 3 for $W \to \mu\nu$ and in Section 7 for $W \to e\nu$. Hadronic jets are reconstructed by clustering charged and neutral hadrons and photons identified by the Particle Flow method. The infrared-safe Anti-kt [35] jet clustering with a cone radius of $\Delta R = 0.5$ is used.

In the Particle Flow procedure stable particles result from combining information from all CMS sub-detectors and are calibrated depending on their type. Small remaining jet energy corrections are applied [36]. We consider jets within the tracker acceptance $|\eta| < 2.5$ with two different energy thresholds: $E_T > 15$ GeV and $E_T > 30$ GeV. Jets must be separated from the closest lepton identified as coming from a boson decay by more than the cone radius used in jet clustering, $\Delta R > 0.5$.

Events are classified according to the number of jets above threshold in an inclusive way: the jet multiplicity bin n gathers events containing n jets or more in addition to the lepton. The signal yield in the electron channel is extracted for each jet multiplicity from an unbinned maximum likelihood fit to the transverse mass distribution. In contrast with the cross-section analysis, the M_T variable is chosen here for both channels because its shape is less sensitive to the presence of hard jets or to situation of large boost of the electroweak boson.

The $t\bar{t}$ background is sizable in jet-multiplicity bins $n \geq 3$. In the electron channel, the ratio of $t\bar{t}$ background with respect to the signal is fixed to the expectation from Monte Carlo simulation. In the muon channel the shape of signal and backgrounds are taken from the Monte Carlo simulation and their normalization is left free to vary in the fit.

The systematic uncertainty on the jet rate above a certain transverse energy threshold is dominated by the jet energy scale. Jet energy scale uncertainties are estimated at the level of $\pm 5\%$ on the absolute scale and of $\pm 2\%$ on the relative scale over the range in pseudo-rapidity [36]. This leads to systematic uncertainties on event counts between 10% and 40% from the one-jet multiplicity bin to the four-jet multiplicity bin for $E_T > 15$ GeV, and between 10% and 20% from the one-jet multiplicity bin to the three-jet multiplicity for $E_T > 30$ GeV. Other sources of systematic uncertainties are being investigated.

Fig. 16 presents the results $N(W \to \ell\nu + \geq n \text{ jets})$ as a function of the inclusive jet multiplicity n, up to $n = 4$ ($n = 3$) for $E_T > 15$ GeV ($E_T > 30$ GeV), in 198 nb^{-1} of integrated luminosity. Electron and muon results are combined. The left side of the figure corresponds to the $E_T > 15$ GeV threshold. The rate of low E_T jets is sensitive to the tuning of the parton shower generator. Here we compare the data with prediction obtained from the PYTHIA generator with different recent tunes [37–39]. The right side of the figure corresponds to the $E_T > 30$ GeV threshold. The rate of high E_T jets is sensitive directly to the matrix element of the hard scattering at the parton level. Here we compare the data with predictions obtained with two different generators, PYTHIA and MADGRAPH [40]. All Monte Carlo predictions are normalized to the NLO inclusive cross section prediction obtained with the MCFM generator [41].

In Fig. 17, we present the p_T spectrum for the hardest jet in the event in events with a W candidate (with a cut $M_T > 50$ GeV) and at least one jet with $E_T > 10$ GeV. In this plot all signal and backgrounds components are taken from the simulation and normalized to the expected cross-sections.

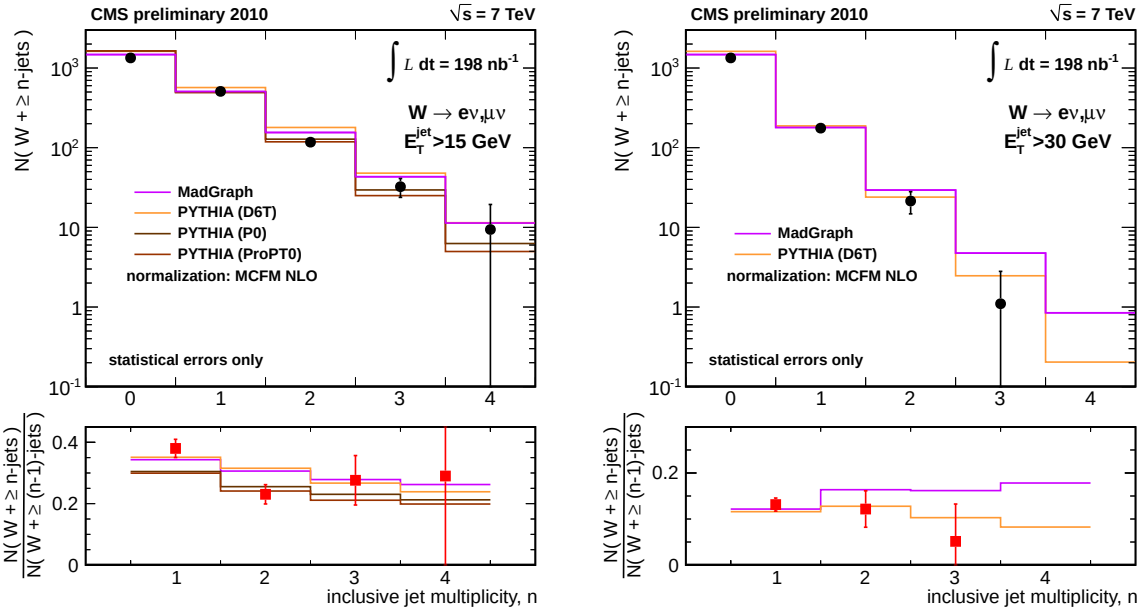

Figure 16: As a function of the inclusive jet multiplicity n, number of $W \to \ell\nu$ events ($\ell = e, \mu$) containing n jets above threshold or more (top plots) and ratio $N(W \to \ell\nu, \geq n\,\text{jets})/N(W \to \ell\nu, \geq (n-1)\,\text{jets})$ (bottom plots). Predictions obtained with PYTHIA (D6T [37]) and MADGRAPH are shown, normalized to the NLO cross section from MCFM. On the left, the jet E_T threshold is 15 GeV; predictions obtained from PYTHIA with different tunes (P0 [38] and ProPT0 [39]) are also shown. On the right, the jet E_T threshold is 30 GeV. The error bars are statistical only.

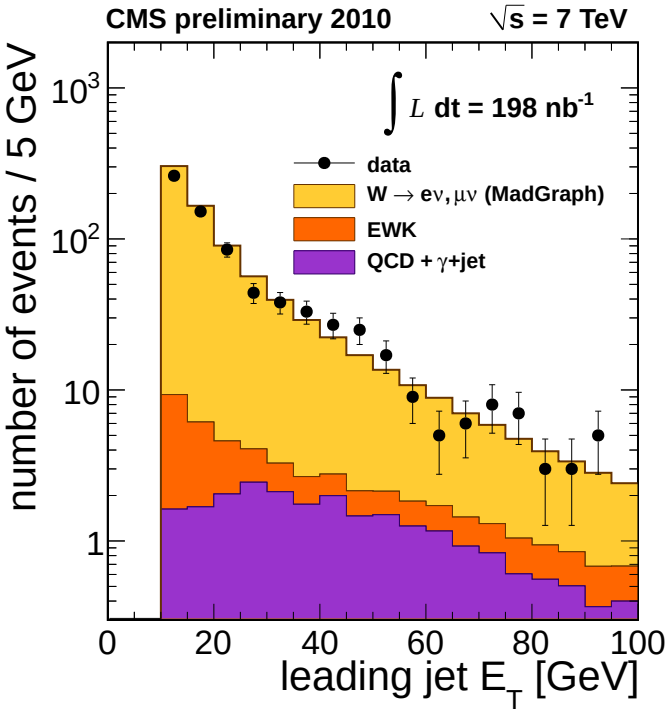

Figure 17: Leading jet p_T for jets in $W \to \mu\nu$ and $W \to e\nu$ events with $M_T > 50$ GeV/c^2. Jets with $E_T > 10$ GeV are considered.

15 Conclusion

First measurements of W and $Z(\gamma^*)$ cross sections have been made using approximately 198 nb^{-1} of data taken with the CMS detector at the LHC. In addition, the W charge asymmetry, A_{FB}, and the rate of producing jets in association with W bosons have been measured. Within large statistical uncertainties, no disagreements with the predictions of the Standard Model have been observed.

References

[1] M. Dittmar, F. Pauss, and D. Zurcher, "Towards a precise parton luminosity determination at the CERN LHC", *Phys. Rev.* **D56** (1997) 7284–7290, arXiv:hep-ex/9705004. doi:10.1103/PhysRevD.56.7284.

[2] A. D. Martin, W. J. Stirling, R. S. Thorne et al., "Parton distributions for the LHC", *Eur. Phys. J.* **C63** (2009) 189–285, arXiv:0901.0002. doi:10.1140/epjc/s10052-009-1072-5.

[3] A. D. Martin, W. J. Stirling, R. S. Thorne et al., "Uncertainties on α_S in global PDF analyses", arXiv:0905.3531.

[4] CDF II Collaboration, "First measurements of inclusive W and Z cross sections from Run II of the Tevatron collider", *Phys. Rev. Lett.* **94** (2005) 091803, arXiv:hep-ex/0406078. doi:10.1103/PhysRevLett.94.091803.

[5] CDF Collaboration, "The transverse momentum and total cross section of e^+e^- pairs in the Z boson region from $p\bar{p}$ collisions at $\sqrt{s} = 1.8$ TeV", *Phys. Rev. Lett.* **84** (2000) 845–850, arXiv:hep-ex/0001021. doi:10.1103/PhysRevLett.84.845.

[6] D0 Collaboration, "Extraction of the width of the W boson from measurements of $\sigma(p\bar{p} \to W + X) \times B(W \to e\nu)$ and $\sigma(p\bar{p} \to Z + X) \times B(Z \to ee)$ and their ratio", *Phys. Rev.* **D61** (2000) 072001, arXiv:hep-ex/9906025. doi:10.1103/PhysRevD.61.072001.

[7] UA2 Collaboration, "Measurement of W and Z Production Cross-Sections at the CERN $\bar{p}p$ Collider", *Z. Phys.* **C47** (1990) 11–22. doi:10.1007/BF01551906.

[8] UA1 Collaboration, "Studies of Intermediate Vector Boson Production and Decay in UA1 at the CERN Proton - Antiproton Collider", *Z. Phys.* **C44** (1989) 15–61. doi:10.1007/BF01548582.

[9] CMS Collaboration, "The CMS experiment at the CERN LHC", JINST 0803:S08004,2008.

[10] CMS Collaboration, "Measurement of CMS luminosity", *CMS PAS* **EWK-2010-004** (2010).

[11] CMS Collaboration, "Particle-flow commissioning with muons and electrons from J/Psi, and W events at 7 TeV", *CMS PAS* **PFT-2010-003** (2010).

[12] CMS Collaboration, "CMS MET Performance in Events Containing Electroweak Bosons from pp Collisions at $\sqrt{s}$=7 TeV", *CMS PAS* **JME-2010-005** (2010).

[13] S. Alioli, P. Nason, C. Oleari et al., "NLO vector-boson production matched with shower in POWHEG", *JHEP* **07** (2008) 060, arXiv:0805.4802. doi:10.1088/1126-6708/2008/07/060.

[14] P. Nason, "A new method for combining NLO QCD with shower Monte Carlo algorithms", *JHEP* **11** (2004) 040, arXiv:hep-ph/0409146. doi:10.1088/1126-6708/2004/11/040.

[15] S. Frixione, P. Nason, and C. Oleari, "Matching NLO QCD computations with Parton Shower simulations: the POWHEG method", *JHEP* **11** (2007) 070, arXiv:0709.2092. doi:10.1088/1126-6708/2007/11/070.

[16] T. Sjostrand, S. Mrenna, and P. Z. Skands, "PYTHIA 6.4 Physics and Manual", *JHEP* **05** (2006) 026, arXiv:hep-ph/0603175.

[17] S. Agostinelli et al., Nucl. Instr. and Methods A 506 (2003) 250-303.

[18] CMS Collaboration, "Performance of CMS muon identification in pp collisions at $\sqrt{s} = 7$ TeV", *CMS PAS* **MUO-2010-002** (2010).

[19] W. Adam et al., *The CMS High Level Trigger*, **Eur. Phys. J. C46 (2006), 605-667**.

[20] CMS Collaboration, "Electron Reconstruction and Identification at $\sqrt{s} = 7$ TeV", *CMS Detector Performance Summary* **DP-2010-032** (2010).

[21] W. Adam et. al., *Reconstruction of Electrons with the Gaussian-Sum Filter in the CMS Tracker at the LHC*, **CMS Note 2005/001**.

[22] P. M. Nadolsky et al., "Implications of CTEQ global analysis for collider observables", *Phys. Rev.* **D78** (2008) 013004, arXiv:0802.0007. doi:10.1103/PhysRevD.78.013004.

[23] R. D. Ball et al., "A first unbiased global NLO determination of parton distributions and their uncertainties", arXiv:1002.4407.

[24] K. Melnikov and F. Petriello, "Electroweak gauge boson production at hadron colliders through O(alpha(s)**2)", *Phys. Rev.* **D74** (2006) 114017, arXiv:hep-ph/0609070. doi:10.1103/PhysRevD.74.114017.

[25] K. Melnikov and F. Petriello, "The W boson production cross section at the LHC through $O(\alpha_s^2)$", *Phys. Rev. Lett.* **96** (2006) 231803, arXiv:hep-ph/0603182. doi:10.1103/PhysRevLett.96.231803.

[26] CMS Collaboration, "Muon Differential Cross Section and Charge Asymmetry in Inclusive $pp \to W(\mu\nu) + X$ Production at $\sqrt{s} = 10$ TeV", **CMS PAS EWK-09-003**.

[27] G. A. Ladinsky and C. P. Yuan, "The Nonperturbative regime in QCD resummation for gauge boson production at hadron colliders", *Phys. Rev.* **D50** (1994) 4239, arXiv:hep-ph/9311341. doi:10.1103/PhysRevD.50.R4239.

[28] C. Balazs, J.-w. Qiu, and C. P. Yuan, "Effects of QCD resummation on distributions of leptons from the decay of electroweak vector bosons", *Phys. Lett.* **B355** (1995) 548–554, arXiv:hep-ph/9505203. doi:10.1016/0370-2693(95)00726-2.

[29] C. Balazs and C. P. Yuan, "Testing multiple gluon dynamics at the Tevatron", *Phys. Rev. Lett.* **79** (1997) 2398–2401, arXiv:hep-ph/9703405. doi:10.1103/PhysRevLett.79.2398.

[30] C. Balazs and C. P. Yuan, "Soft gluon effects on lepton pairs at hadron colliders", *Phys. Rev.* **D56** (1997) 5558–5583, arXiv:hep-ph/9704258. doi:10.1103/PhysRevD.56.5558.

[31] F. Landry, R. Brock, P. M. Nadolsky et al., "Tevatron Run-1 Z boson data and Collins-Soper-Sterman resummation formalism", *Phys. Rev.* **D67** (2003) 073016, arXiv:hep-ph/0212159. doi:10.1103/PhysRevD.67.073016.

[32] A. V. Konychev and P. M. Nadolsky, "Universality of the Collins-Soper-Sterman nonperturbative function in gauge boson production", *Phys. Lett.* **B633** (2006) 710–714, arXiv:hep-ph/0506225. doi:10.1016/j.physletb.2005.12.063.

[33] C. Anastasiou, L. J. Dixon, K. Melnikov et al., "Dilepton rapidity distribution in the Drell-Yan process at NNLO in QCD", *Phys. Rev. Lett.* **91** (2003) 182002, arXiv:hep-ph/0306192. doi:10.1103/PhysRevLett.91.182002.

[34] J. D. Collins and D. E. Soper, "Angular distribution of dileptons in high-energy hadron collisions", *Phys. Rev.* **D16** (1977) 2219–2225.

[35] M. Cacciari, G.P. Salam, and G. Soyez, The anti-kt jet clustering algorithm, JHEP 0804, (2008) 063.

[36] CMS Collaboration, "CMS Jet Performance in pp Collisions at $\sqrt{s} = 7$ TeV", *CMS PAS* **JME-2010-003** (2010).

[37] CDF Collaboration, "The underlying event in hard scattering processes", arXiv:hep-ph/0201192.

[38] P. Z. Skands, "The Perugia Tunes", arXiv:1005.3457.

[39] A. Buckley, H. Hoeth, H. Lacker et al., "Systematic event generator tuning for the LHC", *Eur. Phys. J.* **C65** (2010) 331–357, arXiv:0907.2973. doi:10.1140/epjc/s10052-009-1196-7.

[40] F. Maltoni and T. Stelzer, "MadEvent: Automatic event generation with MadGraph", *JHEP* **02** (2003) 027, arXiv:hep-ex/0208156.

[41] J. Campbell and R.K. Ellis, "Monte Carlo for FeMtobarn processes", http://mcfm.fnal.gov/.

Appendix A. Track-corrected $\not\!\!E_T$ distributions

This Appendix section presents plots of transverse mass (muon channel) and missing transverse energy (electron channel) produced using the track-corrected $\not\!\!E_T$ technique.

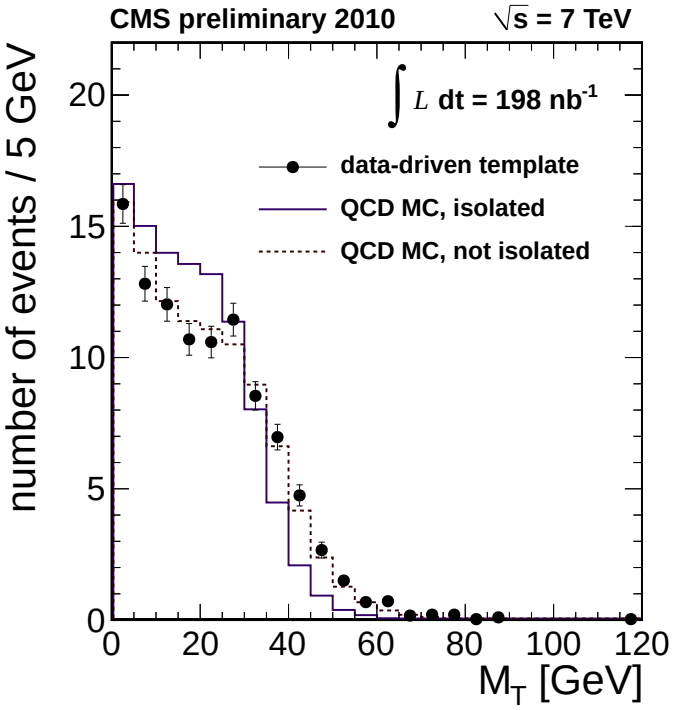

Figure 18: Comparison of the M_T distribution of QCD background in $W \to \mu\nu$ candidates, as derived from isolation inversion in data (points), with the same distribution expected from the simulation (dashed histogram). The Monte Carlo distribution predicted for the selected QCD sample (solid histogram), used to conservatively assign systematic uncertainties, is also shown for comparison.

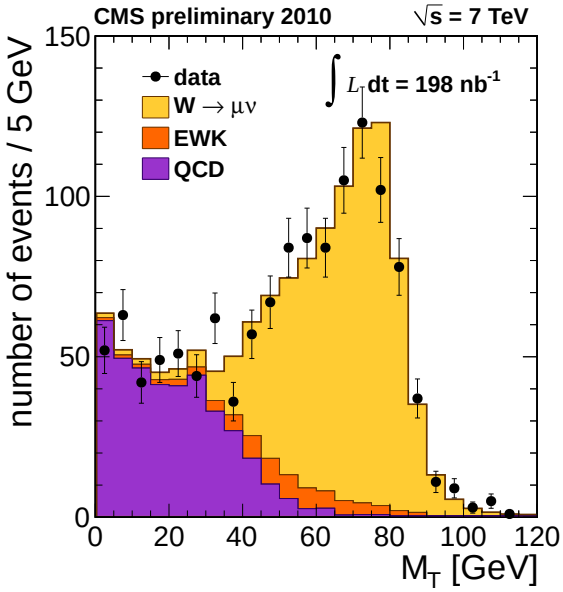

Figure 19: Fit to the M_T spectrum of W candidates (black points) together with the obtained templates for the different processes: W signal, other EWK processes, and QCD background (solid histograms). The signal yield is $N_W = 818 \pm 27$, where the indicated error is statistical only.

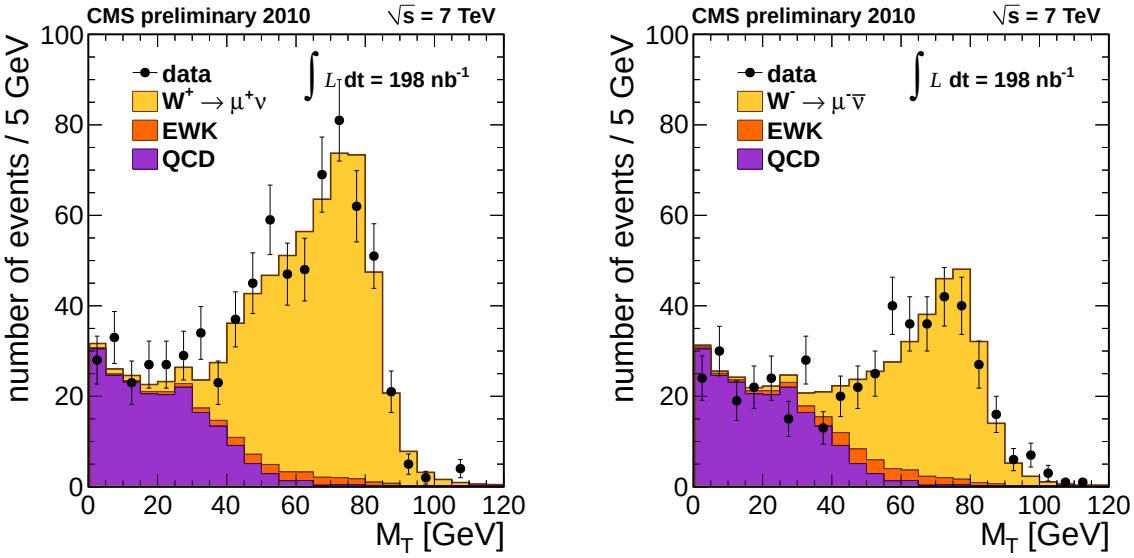

Figure 20: Fits to the M_T spectrum of positive and negative W candidates (black points) together with the obtained templates for the different processes: W signal, other EWK processes, and QCD background (solid histograms). The signal yields are $N_{W^+} = 527 \pm 24$ and $N_{W^-} = 291 \pm 13$, where the indicated errors are statistical only.

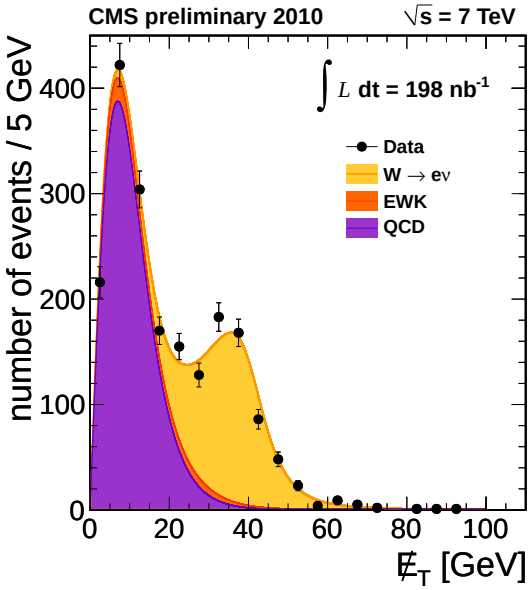

Figure 21: Distribution of $\not\!\!E_T$ for the selected $W \rightarrow e\nu$ candidates in data (points). Superimposed are the results of the likelihood fit for QCD background (violet), all backgrounds (orange), and signal plus background (yellow).

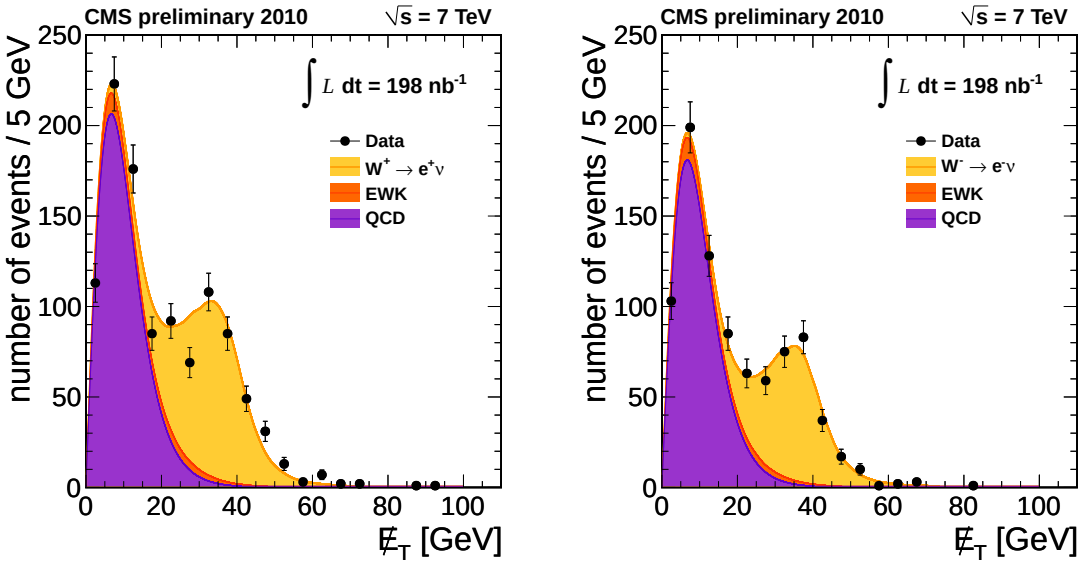

Figure 22: Distribution of $\not\!\!E_T$ for the selected $W^+ \rightarrow e^+\nu$ candidates (left) and $W^- \rightarrow e^-\overline{\nu}$ candidates (right) in data (points). Superimposed are the results of a simultaneous likelihood fit for QCD background (violet), all backgrounds (orange), and signals plus background (yellow).

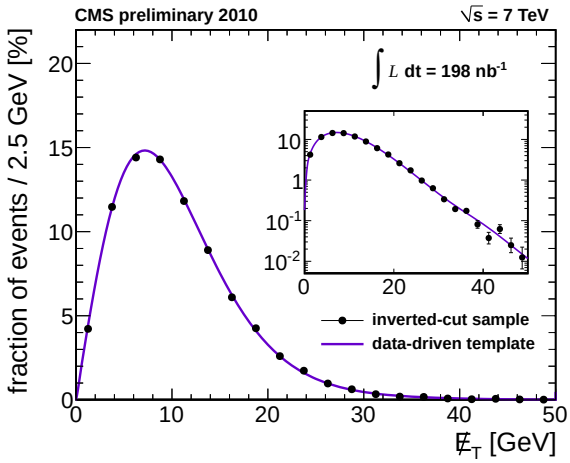

Figure 23: Distribution of $\not\!\!E_{\mathrm{T}}$ for a background-dominated sample of events in the data failing the cluster/track matching requirements of the $\mathrm{W} \to \mathrm{e}\nu$ candidate selection, with only ECAL isolation applied (points). The result of the fit (superimposed in dark blue) is used to fix the parameter σ_1 of the QCD background shape.